

The Mass Ratio Distribution of Tertiary Induced Binary Black Hole Mergers

Yubo Su,^{1*} Bin Liu,^{1,2} Dong Lai^{1,3}

¹ *Cornell Center for Astrophysics and Planetary Science, Department of Astronomy, Cornell University, Ithaca, NY 14853, USA*

² *Niels Bohr International Academy, Niels Bohr Institute, Blegdamsvej 17, 2100 Copenhagen, Denmark*

³ *Tsung-Dao Lee Institute & School of Physics and Astronomy, Shanghai Jiao Tong University, 200240 Shanghai, China*

Accepted June 02, 2021. Received March 02, 2021; in original form March 02, 2021

ABSTRACT

Many proposed scenarios for black hole (BH) mergers involve a tertiary companion that induces von Zeipel-Lidov-Kozai (ZLK) eccentricity cycles in the inner binary. An attractive feature of such mechanisms is the enhanced merger probability when the octupole-order effects, also known as the eccentric Kozai mechanism, are important. This can be the case when the tertiary is of comparable mass to the binary components. Since the octupole strength $[\propto (1 - q)/(1 + q)]$ increases with decreasing binary mass ratio q , such ZLK-induced mergers favor binaries with smaller mass ratios. We use a combination of numerical and analytical approaches to fully characterize the octupole-enhanced binary BH mergers and provide semi-analytical criteria for efficiently calculating the strength of this enhancement. We show that for hierarchical triples with semi-major axis ratio $a/a_{\text{out}} \gtrsim 0.01\text{--}0.02$, the binary merger fraction can increase by a large factor (up to ~ 20) as q decreases from unity to 0.2. The resulting mass ratio distribution for merging binary BHs produced in this scenario is in tension with the observed distribution obtained by the LIGO/VIRGO collaboration, although significant uncertainties remain about the initial distribution of binary BH masses and mass ratios.

Key words: binaries:close – stars:black holes

1 INTRODUCTION

The 50 or so black hole (BH) binary mergers detected by the LIGO/VIRGO collaboration to date (Abbott et al. 2020a) continue to motivate theoretical studies of their formation channels. These range from the traditional isolated binary evolution, in which mass transfer and friction in the common envelope phase cause the binary orbit to decay sufficiently that it subsequently merges via emission of gravitational waves (GWs) (e.g., Lipunov et al. 1997, 2017; Podsiadlowski et al. 2003; Belczynski et al. 2010, 2016; Dominik et al. 2012, 2013, 2015), to various flavors of dynamical formation channels that involve either strong gravitational scatterings in dense clusters (e.g., Portegies Zwart & McMillan 2000; O’leary et al. 2006; Miller & Lauburg 2009; Banerjee et al. 2010; Downing et al. 2010; Ziosi et al. 2014; Rodriguez et al. 2015; Samsing & Ramirez-Ruiz 2017; Samsing & D’Orazio 2018; Rodriguez et al. 2018; Gondán et al. 2018) or mergers in isolated triple and quadruple systems induced by distant companions (e.g., Miller & Hamilton 2002; Wen 2003; Antonini & Perets 2012a; Antonini et al. 2017; Silsbee & Tremaine 2017; Liu & Lai 2017, 2018; Randall & Xianyu 2018a,b; Hoang et al. 2018; Fragione & Kocsis 2019; Fragione & Loeb 2019; Liu & Lai 2019; Liu et al. 2019a,b; Liu & Lai 2020; Liu & Lai 2021).

Given the large number of merger events to be detected in the coming years, it is important to search for observational signatures to distinguish various BH binary formation channels. The masses of merging BHs obviously carry important information. The recent

detection of BH binary systems with component masses in the mass gap (such in GW190521) suggests that some kinds of “hierarchical mergers” may be needed to explain these exceptional events (Abbott et al. 2020b; see Liu & Lai 2021 for examples of such “hierarchical mergers” in stellar multiples). Another possible indicator is merger eccentricity: previous studies find that dynamical binary-single interactions in dense clusters (e.g., Samsing & Ramirez-Ruiz 2017; Rodriguez et al. 2018; Samsing & D’Orazio 2018; Fragione & Bromberg 2019) or in galactic triples (Silsbee & Tremaine 2017; Antonini et al. 2017; Fragione & Loeb 2019; Liu et al. 2019a) may lead to BH binaries that enter the LIGO band with modest eccentricities. The third possible indicator is the spin-orbit misalignment of the binary. In particular, the mass-weighted projection of the BH spins,

$$\chi_{\text{eff}} = \frac{m_1 \chi_1 + m_2 \chi_2}{m_1 + m_2} \cdot \hat{\mathbf{L}}, \quad (1)$$

can be measured through the binary inspiral waveform [here, $m_{1,2}$ is the BH mass, $\chi_{1,2} = cS_{1,2}/(Gm_{1,2}^2)$ is the dimensionless BH spin, and $\hat{\mathbf{L}}$ is the unit orbital angular momentum vector of the binary]. Different formation histories yield different distributions of χ_{eff} (Liu & Lai 2017, 2018; Antonini et al. 2018; Rodriguez et al. 2018; Gerosa et al. 2018; Liu et al. 2019a; Su et al. 2021).

The fourth possible indicator of BH binary formation mechanisms is the distribution of masses and mass ratios of merging BHs. In Fig. 1, we show the distribution of the mass ratio $q \equiv m_2/m_1$, where $m_1 \geq m_2$, for all LIGO/VIRGO binaries detected as of the O3a

* E-mail: yubosu@astro.cornell.edu

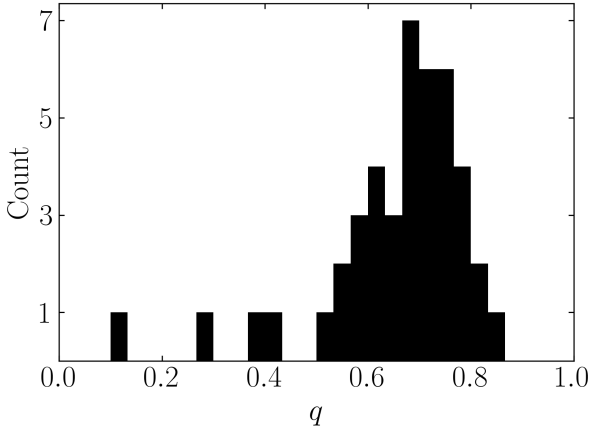


Figure 1. Histogram of the mass ratios $q \equiv m_2/m_1$ of binary BH mergers in the O3a data release, excluding the two NS-NS mergers but including GW190814, whose $2.5M_\odot$ secondary may be a BH (Abbott et al. 2020a).

data release (Abbott et al. 2020a)¹. The distribution distinctly peaks around $q \sim 0.7$. BH binaries formed via isolated binary evolution are generally expected to have $q \gtrsim 0.5$ (Belczynski et al. 2016; Olejak et al. 2020). On the other hand, dynamical formation channels may produce a larger variety of distributions for the binary mass ratio (e.g., Rodriguez et al. 2016; Silsbee & Tremaine 2017; Fragione & Kocsis 2019).

In this paper, we study in detail the mass ratio distribution for BH mergers induced by tertiary companions in isolated triple systems. In this scenario, a tertiary BH on a sufficiently inclined (outer) orbit induces phases of extreme eccentricity in the inner binary via the von Zeipel-Lidov-Kozai (ZLK; von Zeipel 1910; Lidov 1962; Kozai 1962) effect, leading to efficient gravitational radiation and orbital decay. While the original ZLK effect relies on the leading-order, quadrupolar gravitational perturbation from the tertiary on the inner binary, the octupole order terms can become important (sometimes known as the eccentric Kozai mechanism, e.g. Naoz 2016) when the triple system is mildly hierarchical, the outer orbit is eccentric ($e_{\text{out}} \neq 0$) and the inner binary BHs have unequal masses (e.g., Ford et al. 2000; Blaes et al. 2002; Lithwick & Naoz 2011; Liu et al. 2015). The strength of the octupole effect depends on the dimensionless parameter

$$\epsilon_{\text{oct}} = \frac{m_1 - m_2}{m_1 + m_2} \frac{a}{a_{\text{out}}} \frac{e_{\text{out}}}{1 - e_{\text{out}}^2}. \quad (2)$$

where a , a_{out} are the semi-major axes of the inner and outer binaries, respectively. Previous studies have shown that the octupole terms generally increase the inclination window for extreme eccentricity excitation, and thus enhance the rate of successful binary mergers (Liu & Lai 2018). As $\epsilon_{\text{oct}} \propto (1 - q)/(1 + q)$ increases with decreasing q , we expect that ZLK-induced BH mergers favor binaries with smaller mass ratios. The main goal of this paper is to quantify the

dependence of the merger fraction/probability on q , using a combination of analytical and numerical calculations. We focus on the cases where the tertiary mass is comparable to the binary BH masses. When the tertiary mass m_3 is much larger than $m_{12} = m_1 + m_2$ (as in the case of a supermassive BH tertiary), dynamical stability of the triple requires $a_{\text{out}}(1 - e_{\text{out}})/[a(1 + e)] \gtrsim 3.7(m_3/m_{12})^{1/3} \gg 1$ (Kiseleva et al. 1996), which implies that the octupole effect is negligible.

This paper is organized as follows. In Section 2, we review some analytical results of ZLK oscillations and examine how the octupole terms affect the inclination window and probability for extreme eccentricity excitation. In Section 3, we study tertiary-induced BH mergers using a combination of numerical and analytical approaches. We propose new semi-analytical criteria (Section 3.2) that allow us to determine, without full numerical integration, whether an initial BH binary can undergo a “one-shot merger” or a more gradual merger induced by the octupole effect of a tertiary. In Section 4, we calculate the merger fraction as a function of mass ratio for some representative triple systems. In Section 5, we study the mass ratio distribution of the initial BH binaries based on the properties of main-sequence (MS) stellar binaries and the MS mass to BH mass mapping. Using the result of Section 4, we illustrate how the final merging BH binary mass distribution may be influenced by the octupole effect for tertiary-induced mergers. We summarize our results and their implications in Section 6.

2 VON ZEIPEL-LIDOV-KOZAI (ZLK) OSCILLATIONS: ANALYTICAL RESULTS

Consider two BHs orbiting each other with masses m_1 and m_2 on a orbit with semi-major axis a , eccentricity e , and angular momentum \mathbf{L} . An external, tertiary BH of mass m_3 orbits this inner binary with semi-major axis a_{out} , eccentricity e_{out} , and angular momentum \mathbf{L}_{out} . The reduced masses of the inner and outer binaries are $\mu \equiv m_1 m_2 / m_{12}$ and $\mu_{\text{out}} \equiv m_1 m_3 / m_{123}$ respectively, where $m_{12} = m_1 + m_2$ and $m_{123} = m_{12} + m_3$. These two binary orbits are further described by three angles: the inclinations i and i_{out} , the arguments of pericenters ω and ω_{out} , and the longitudes of the ascending nodes Ω and Ω_{out} . These angles are defined in a coordinate system where the z axis is aligned with the total angular momentum $\mathbf{J} = \mathbf{L} + \mathbf{L}_{\text{out}}$ (i.e., the invariant plane is perpendicular to \mathbf{J}). The mutual inclination between the two orbits is denoted $I \equiv i + i_{\text{out}}$. Note that $\Omega_{\text{out}} = \Omega + 180^\circ$.

To study the evolution of the inner binary under the influence of the tertiary BH, we use the double-averaged secular equations of motion, including the interactions between the inner binary and the tertiary up to the octupole level of approximation as given by Liu et al. (2015). Throughout this paper, we restrict to hierarchical triple systems where the double-averaged secular equations are valid – systems with relatively small a_{out}/a may require solving the single-averaged equations of motion or direct N-body integration (see Antonini & Perets 2012b; Antonini et al. 2014; Luo et al. 2016; Lei et al. 2018; Liu & Lai 2019; Liu et al. 2019a; Hamers 2020a)². For the remainder of this section, we include general relativistic apsidal precession of the inner binary, a first order post-Newtonian (1PN) effect, but omit

¹ Note that Fig. 1 should not be interpreted as directly reflecting the distribution of merging BH binaries, as there are many selection effects and observational biases, e.g. systems with smaller q are harder to detect for the same M_{chirp} or m_{12} . For a detailed statistical analysis, see Abbott et al. (2020a).

² Although we do not study such systems in this paper, we expect that a qualitatively similar dependence of the merger probability on the mass ratio remains, since the strength of the octupole effect in the single-averaged secular equations is also proportional to $(1 - q)/(1 + q)$ (see Eq. 25 of Liu & Lai 2019).

the emission of GWs, a 2.5PN effect – this will be considered in Section 3. We group the results by increasing order of approximation, starting by ignoring the octupole-order effects entirely.

2.1 Quadrupole Order

At the quadrupole order, the tertiary induces eccentricity oscillations in the inner binary on the characteristic timescale

$$t_{\text{ZLK}} = \frac{1}{n} \frac{m_{12}}{m_3} \left(\frac{a_{\text{out,eff}}}{a} \right)^3, \quad (3)$$

where $n \equiv \sqrt{Gm_{12}/a^3}$ is the mean motion of the inner binary, and $a_{\text{out,eff}} \equiv a_{\text{out}} \sqrt{1 - e_{\text{out}}^2}$. During these oscillations, there are two conserved quantities, the total energy and the total orbital angular momentum. Through some manipulation, the total angular momentum can be written in terms of the conserved quantity K given by

$$K \equiv j(e) \cos I - \frac{\eta}{2} e^2. \quad (4)$$

Here, $j(e) \equiv \sqrt{1 - e^2}$ and η is the ratio of the magnitudes of the angular momenta at zero inner binary eccentricity:

$$\eta \equiv \left(\frac{L}{L_{\text{out}}} \right)_{e=0} = \frac{\mu}{\mu_{\text{out}}} \left[\frac{m_{12}a}{m_{12}3a_{\text{out}}(1 - e_{\text{out}}^2)} \right]^{1/2}. \quad (5)$$

Note that when $\eta = 0$, K reduces to the classical “Kozai constant”, $K = j(e) \cos I$.

The maximum eccentricity e_{max} attained in these ZLK oscillations can be computed analytically at the quadrupolar order. It depends on the “competition” between the 1PN apsidal precession rate $\dot{\omega}_{\text{GR}}$ and the ZLK rate t_{ZLK}^{-1} . The relevant dimensionless parameter is

$$\epsilon_{\text{GR}} \equiv (\dot{\omega}_{\text{GR}} t_{\text{ZLK}})_{e=0} = \frac{3Gm_{12}}{c^2} \frac{m_{12}}{m_3} \frac{a_{\text{out,eff}}^3}{a^4}. \quad (6)$$

It can then be shown that, for an initially circular inner binary, e_{max} is related to the initial mutual inclination I_0 by (Liu et al. 2015; Anderson et al. 2016):

$$\frac{3}{8} \frac{j^2(e_{\text{max}}) - 1}{j^2(e_{\text{max}})} \left[5 \left(\cos I_0 + \frac{\eta}{2} \right)^2 - \left(3 + 4\eta \cos I_0 + \frac{9}{4}\eta^2 \right) j^2(e_{\text{max}}) + \eta^2 j^4(e_{\text{max}}) \right] + \epsilon_{\text{GR}} \left[1 - \frac{1}{j(e_{\text{max}})} \right] = 0. \quad (7)$$

In the limit $\eta \rightarrow 0$ and $\epsilon_{\text{GR}} \rightarrow 0$, we recover the well-known result $e_{\text{max}} = \sqrt{1 - (5/3) \cos^2 I_0}$. For general η , e_{max} attains its limiting value e_{lim} when $I_0 = I_{0,\text{lim}}$, where (see also Hamers 2020b)

$$\cos I_{0,\text{lim}} = \frac{\eta}{2} \left[\frac{4}{5} j^2(e_{\text{lim}}) - 1 \right]. \quad (8)$$

Note that $I_{0,\text{lim}} \geq 90^\circ$ with equality only when $\eta = 0$. Substituting Eq. (8) into Eq. (7), we find that e_{lim} satisfies

$$\frac{3}{8} \left[j^2(e_{\text{lim}}) - 1 \right] \left[-3 + \frac{\eta^2}{4} \left(\frac{4}{5} j^2(e_{\text{lim}}) - 1 \right) \right] + \epsilon_{\text{GR}} \left[1 - \frac{1}{j(e_{\text{lim}})} \right] = 0. \quad (9)$$

On the other hand, eccentricity excitation ($e_{\text{max}} \geq 0$) is only possible when $(\cos I_0)_- \leq \cos I_0 \leq (\cos I_0)_+$ where

$$(\cos I_0)_\pm = \frac{1}{10} \left(-\eta \pm \sqrt{\eta^2 + 60 - \frac{80}{3} \epsilon_{\text{GR}}} \right). \quad (10)$$

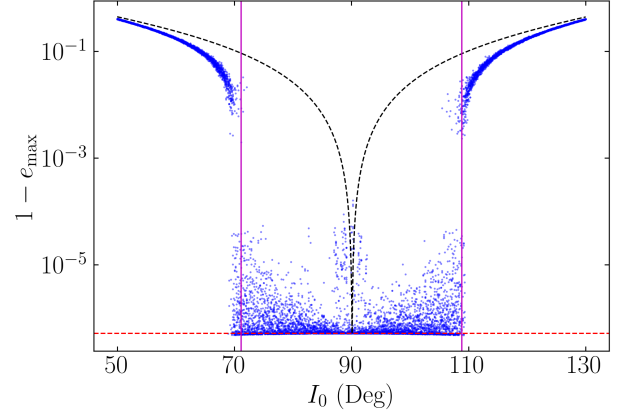


Figure 2. The maximum eccentricity achieved for an inner binary in the test-particle limit as a function of the initial inclination angle I_0 . The triple system parameters are: $a = 100$ AU, $a_{\text{out,eff}} = 3600$ AU, $m_{12} = 50M_\odot$, $m_3 = 30M_\odot$, and $e_{\text{out}} = 0.6$; the corresponding octupole strength parameter is $\epsilon_{\text{oct}} = 0.02$ and $\eta \approx 0$. The octupole-level secular equations of motion are integrated for $2000t_{\text{ZLK}}$ (see Eq. 3), and the maximum eccentricity attained during this time is recorded and shown as a blue dot for each initial condition. We consider 1000 initial inclinations in the range $50^\circ \leq I_0 \leq 130^\circ$, and each I_0 is simulated five times, with the initial orbital elements ω , ω_{out} , and $\Omega = \Omega_{\text{out}} - \pi$ chosen randomly $\in [0, 2\pi)$ for each simulation. The dotted black line shows the quadrupole-level result (Eq. 7 with $\eta = 0$), and e_{lim} (Eq. 9) is shown as the horizontal red line. The vertical purple lines denote the boundary of the octupole-active inclination window, based on the fitting formula from Muñoz et al. (2016) (Eq. 12).

For I_0 outside of this range, no eccentricity excitation is possible. This condition reduces to the well-known $\cos^2 I_0 \leq 3/5$ when $\eta = \epsilon_{\text{GR}} = 0$.

2.2 Octupole Order: Test-particle Limit

The relative strength of the octupole-order potential to the quadrupole-order potential is determined by the dimensionless parameter ϵ_{oct} (Eq. 2). When ϵ_{oct} is non-negligible, K is no longer conserved, and the system evolution becomes chaotic (Ford et al. 2000; Katz et al. 2011; Lithwick & Naoz 2011; Li et al. 2014; Liu et al. 2015). As a result, analytical (and semi-analytical) results have only been given for the test-particle limit, where $m_2 = \eta = 0$. We briefly review these results below.

Due to the non-conservation of K , e_{max} evolves irregularly ZLK cycles, and the orbit may even flip between prograde ($I < 90^\circ$) and retrograde ($I > 90^\circ$) if K changes sign (in the test-particle limit, $K = j(e) \cos I$). During these orbit flips, the eccentricity maxima reach their largest values but do not exceed e_{lim} (Lithwick & Naoz 2011; Liu et al. 2015; Anderson et al. 2016). These orbit flips occur on characteristic timescale $t_{\text{ZLK,oct}}$, given by (Antognini 2015)

$$t_{\text{ZLK,oct}} = t_{\text{ZLK}} \frac{128\sqrt{10}}{15\pi\sqrt{\epsilon_{\text{oct}}}}. \quad (11)$$

The octupole potential tends to widen the inclination range for which the eccentricity can reach e_{lim} ; we refer to this widened range as the *octupole-active window*. Figure 2 shows the maximum eccentricity attained by an inner binary orbited by a tertiary companion with inclination I_0 . The octupole-active window is visible as a range of inclinations centered on $I_0 = 90^\circ$ that attain e_{lim} (the red horizontal

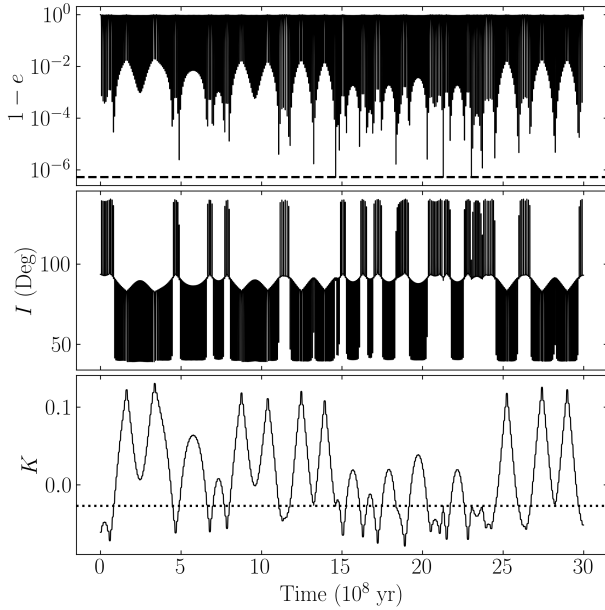


Figure 3. An example of the triple evolution for a system with significant octupole effects and finite η (see Eq. 5). We use the same system parameters as in Fig. 2 except for $q = 0.2$, corresponding to $\eta \approx 0.087$ and $\epsilon_{\text{oct}} \approx 0.007$, and $I_0 = 93.5^\circ$. The three panels show the inner orbit eccentricity, the mutual inclination, and the generalized “Kozai constant” K (Eq. 4). In the first panel, e_{lim} is denoted by the black dashed line. By comparing the second and third panels, we see that orbit flips occur when K crosses the dotted line, given by $K = K_c \equiv -\eta/2$.

dashed line in Fig. 2). Katz et al. (2011) show that this window can be approximated using analytical arguments when $\epsilon_{\text{oct}} \ll 1$. Muñoz et al. (2016) give a more general numerical fitting formula describing the octupole-active window for arbitrary ϵ_{oct} . They find that orbit flips and extreme eccentricity excitation occur for $I_{\text{flip},-} \lesssim I_0 \lesssim I_{\text{flip},+}$ where

$$\cos^2 I_{\text{flip},\pm} = \begin{cases} 0.26 \left(\frac{\epsilon_{\text{oct}}}{0.1} \right) - 0.536 \left(\frac{\epsilon_{\text{oct}}}{0.1} \right)^2 \\ + 12.05 \left(\frac{\epsilon_{\text{oct}}}{0.1} \right)^3 - 16.78 \left(\frac{\epsilon_{\text{oct}}}{0.1} \right)^4 & \epsilon_{\text{oct}} \lesssim 0.05, \\ 0.45 & \epsilon_{\text{oct}} \gtrsim 0.05. \end{cases} \quad (12)$$

In Fig. 2, we see that with the octupole effect included, e_{max} indeed attains e_{lim} when I_0 is within the broad octupole-active window given by Eq. (12) (denoted by the vertical purple lines in Fig. 2).

2.3 Octupole Order: General Masses

For general inner binary masses, when the angular momentum ratio η is non-negligible, the octupole-level ZLK behavior is less well-studied (see Liu et al. 2015). Figure 3 shows an example of the evolution of a triple system with significant η and ϵ_{oct} . Many aspects of the evolution discussed in Section 2.2 are still observed: the ZLK eccentricity maxima and K evolve over timescales $\gg t_{\text{ZLK}}$; the eccentricity never exceeds e_{lim} ; when K crosses $K_c \equiv -\eta/2$, an orbit flip occurs (this follows by inspection of Eq. 4).

However, Eq. (12) no longer describes the octupole-active window as η is non-negligible (see also Rodet et al. 2021). In the top panel of Fig. 4, the blue dots show the maximum achieved eccentricity

of a system with the same parameters as Fig. 2 except with $q = 0.5$ (so $\epsilon_{\text{oct}} = 0.007$ and $\eta = 0.087$). Here, it can be seen that no prograde systems can attain e_{lim} , and only a small range of retrograde inclinations $\geq I_{0,\text{lim}}$ (see Eq. 8) are able to reach e_{lim} . In fact, there is even a clear double valued feature around $I \approx 75^\circ$ in the top panel of Fig. 4 that is not present in Fig. 2. If q is decreased to 0.3 (Fig. 5) or further to 0.2 (Fig. 6), ϵ_{oct} increases while η decreases. This permits a larger number of prograde systems to reach e_{lim} , though a small range of inclinations near $I_0 = 90^\circ$ still do not reach e_{lim} ; we call this range of inclinations the “octupole-inactive gap”. On the other hand, if q is held at 0.5 as in Fig. 4 and e_{out} is increased to 0.9 while holding $a_{\text{out,eff}} = 3600$ AU constant, both ϵ_{oct} and η increase; the top panel of Fig. 7 shows that prograde systems still fail to reach e_{lim} for these parameters, despite the increase in ϵ_{oct} . The top panel of Fig. 8 illustrates the behavior when the inner binary is substantially more compact ($a = 10$ AU): even though ϵ_{oct} is larger than it is in any of Figs. 4–7, we see that prograde perturbers fail to attain e_{lim} . All of these examples (top panels of Figs. 4–8) illustrate importance of η in determining the range of inclinations for the system to be able to reach e_{lim} .

In general, we find that a symmetric octupole-active window (as in Eq. 12) can be realized for sufficiently small η . Rodet et al. (2021) considered some examples of triple systems (consisting of MS stars with planetary companions and tertiaries, for which the short-range forces is dominated by tidal interaction) and found that $\eta \lesssim 0.1$ is sufficient for a symmetric octupole-active window. In the cases considered in this paper, a smaller η is necessary (e.g., $\eta \approx 0.054$ in Fig. 6). Thus, the critical η above which the symmetry of the octupole-active window is significantly broken likely depends on the dominant short-range forces and e_{lim} [in Rodet et al. (2021), $1 - e_{\text{lim}} \sim 10^{-3}$, while in Figs. 2 and 4–8, $1 - e_{\text{lim}} \lesssim 10^{-5}$]. In general, when η is non-negligible, there are up to two octupole-active windows: a prograde window whose existence depends on the specific values of η and ϵ_{oct} , and a retrograde window that always exists.

3 TERTIARY-INDUCED BLACK HOLE MERGERS

Emission of gravitational waves (GWs) affects the evolution of the inner binary, which can be incorporated into the secular equations of motion for the triple (e.g., Peters 1964; Liu & Lai 2018). The associated orbital and eccentricity decay rates are (Peters 1964):

$$\frac{1}{a} \frac{da}{dt} \Big|_{\text{GW}} \equiv -\frac{1}{t_{\text{GW}}} = -\frac{64}{5} \frac{G^3 \mu m_{12}^2}{c^5 a^4 j^7(e)} \left(1 + \frac{73}{24} e^2 + \frac{37}{96} e^4 \right), \quad (13)$$

$$\frac{de}{dt} \Big|_{\text{GW}} = -\frac{304}{15} \frac{G^3 \mu m_{12}^2}{c^5 a^4} \frac{1}{j^5(e)} \left(1 + \frac{121}{304} e^2 \right). \quad (14)$$

GW emission can cause the orbit to decay significantly when extreme eccentricities are reached during the ZLK cycles described in the previous section. This allows even wide binaries (~ 100 AU) to merge efficiently within a Hubble time. While various numerical examples of such tertiary-induced mergers have been given before (e.g., Liu & Lai (2018); see also Liu et al. (2019a) for “population synthesis”), in this section we examine the dynamical process in detail in order to develop an analytical understanding. Our fiducial system parameters are as in Fig. 3: $a_{\text{out,eff}} = 4500$ AU, $e_{\text{out}} = 0.6$, $m_{12} = 50 M_\odot$ (with varying q), $m_3 = 30 M_\odot$, and the inner binary has initial $a_0 = 100$ AU and $e_0 = 10^{-3}$.

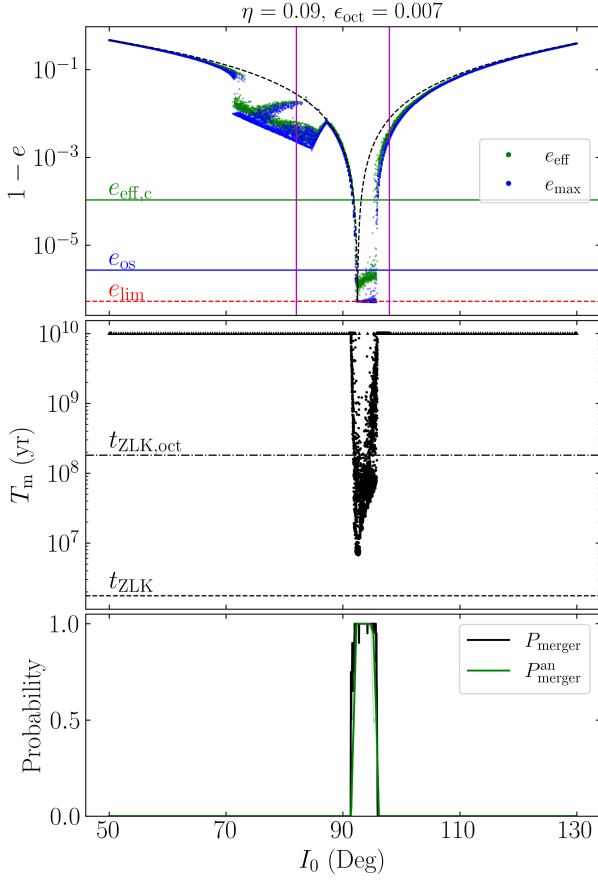


Figure 4. Eccentricity excitation and merger windows for the fiducial BH triple system ($a = 100$ AU, $a_{\text{out,eff}} = 3600$ AU, $m_{12} = 50M_{\odot}$, $m_3 = 30M_{\odot}$) with $q = 0.5$ and $e_{\text{out}} = 0.6$, corresponding to $\eta \approx 0.087$ and $\epsilon_{\text{oct}} \approx 0.007$. In the top panel, for each of 1000 initial inclinations, we choose 5 different random ω , ω_{out} , and Ω as initial conditions and evolve the system for $2000t_{\text{ZLK}}$ without GW radiation. The effective eccentricity e_{eff} (Eq. 21; green dots) as well as the maximum eccentricity e_{max} (blue dots) over this period are displayed. For comparison, $e_{\text{eff,c}}$ (Eq. 22) is given by the horizontal green dashed line, e_{os} (Eq. 18) is shown as the horizontal blue line, and e_{lim} (Eq. 9) is shown as the horizontal red dashed line. The vertical purple lines denote the test-mass octupole-active window and are given by the fitting formula of Muñoz et al. (2016); they do not longer accurately describe the e_{lim} -attaining inclination window because η is finite. The black dashed line is the quadrupole-level result as given by Eq. (7). In the middle panel, we show the binary merger times when including GW radiation and using the same range of initial conditions. Numerical integrations are terminated when $T_{\text{m}} > 10$ Gyr and marked as unsuccessful mergers. The horizontal dashed line denotes t_{ZLK} (Eq. 3) while the horizontal dash-dotted line indicates $t_{\text{ZLK,oct}}$ (Eq. 11). Here, each I_0 is run 20 times with uniform distributions of ω , ω_{out} , and Ω , so we can estimate the merger probability P_{merger} (Eq. 16) for each I_0 – P_{merger} is shown as the black line in the bottom panel. As described in Section 3.2, the merger probability can be predicted semi-analytically using the results of the top panel and Eq. (24), and is denoted by $P_{\text{merger}}^{\text{an}}$. In the bottom panel, the thick green line shows $P_{\text{merger}}^{\text{an}}$ when using an integration time of $2000t_{\text{ZLK}} \approx 3$ Gyr for the non-dissipative simulations, and thin green line shows the prediction using an integration time of $500t_{\text{ZLK}}$. The agreement of $P_{\text{merger}}^{\text{an}}$ with P_{merger} is good and improves when using the longer integration time.

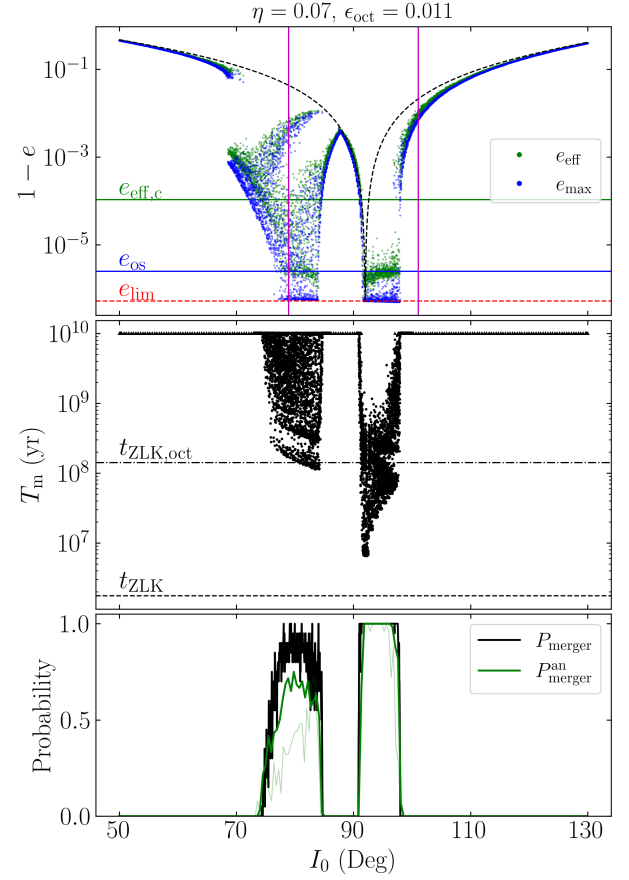


Figure 5. Same as Fig. 4 but for $q = 0.3$, corresponding to $\eta \approx 0.07$ and $\epsilon_{\text{oct}} \approx 0.011$.

3.1 Merger Windows and Probability: Numerical Results

To understand what initial conditions lead to successful mergers within a Hubble time, we integrate the double-averaged octupole-order ZLK equations including GW radiation. We terminate each integration if either $a = 0.005a_0$ (a successful merger) or the system age reaches 10 Gyr. We can verify that the inner binary is effectively decoupled from the tertiary for this orbital separation by evaluating ϵ_{GR} (Eq. 6):

$$\epsilon_{\text{GR}} = 1.8 \times 10^6 \left(\frac{m_{12}}{50M_{\odot}} \right)^2 \left(\frac{a_{\text{out,eff}}}{3600 \text{ AU}} \right)^3 \left(\frac{m_3}{30M_{\odot}} \right)^{-1} \left(\frac{a}{0.5 \text{ AU}} \right)^{-4}. \quad (15)$$

The middle panel of Fig. 4 shows the merger time T_{m} as a function of I_0 for our fiducial parameters with $q = 0.5$. We note that only retrograde inclinations lead to successful mergers, and almost all successful mergers are rapid, with $T_{\text{m}} \sim t_{\text{ZLK,oct}}$. These are the result of a system merging by emitting a single large burst of GW radiation during an extreme-eccentricity ZLK cycle, which we term a “one-shot merger”³. In Fig. 5, q is decreased to 0.3, and some prograde systems are also able to merge successfully. However, these prograde

³ It is important to note that these “one-shot mergers” are distinct from the “fast” mergers previously discussed in the literature (e.g. Wen 2003; Randall & Xianyu 2018b; Su et al. 2021): The one-shot mergers discussed here occur

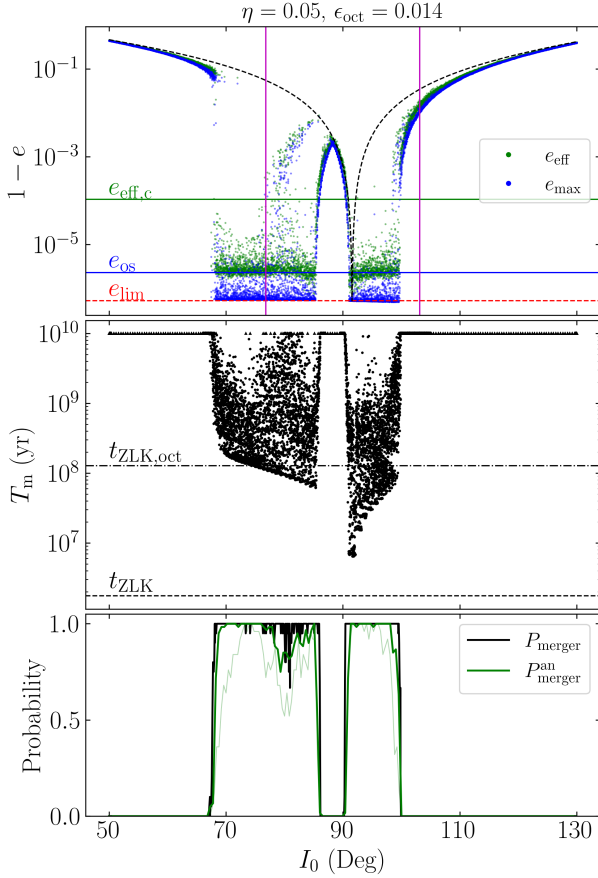


Figure 6. Same as Fig. 4 but for $q = 0.2$, corresponding to $\eta \approx 0.054$ and $\epsilon_{\text{oct}} \approx 0.014$.

systems exhibit a broad range of merger times, with $T_m \gtrsim t_{\text{ZLK,oct}}$. These occur when a system gradually emits a small amount of GW radiation at every eccentricity maximum – we term this a “*smooth merger*”. Additionally, the octupole-inactive gap near $I_0 = 90^\circ$ is visible in the merger time plot (middle panel of Fig. 5). The middle panels of Figs. 6–8 show the behavior of T_m for the other parameter regimes and also exhibit these two categories of mergers and the octupole-inactive gap.

Due to the chaotic nature of the octupole-order ZLK effect, the initial inclination I_0 alone is not sufficient to determine with certainty whether a system can merge within a Hubble time. Instead, for a given I_0 , we can use numerical integrations with various ω , ω_{out} , and Ω to compute a merger probability, denoted by

$$P_{\text{merger}}(I_0; q, e_{\text{out}}) = P(T_m < 10 \text{ Gyr}), \quad (16)$$

when the maximum eccentricity attained by the inner binary over an *octupole* cycle (i.e. within the first $\sim t_{\text{ZLK,oct}}$) is sufficiently large to produce a prompt merger, while the references cited above neglect octupole-order effects and study the scenario when the maximum eccentricity attained in a *quadrupole* ZLK cycle (i.e. within the first $\sim t_{\text{ZLK}}$) is sufficiently large to produce a prompt merger. When the octupole effect is non-negligible, it can drive systems to much more extreme eccentricities than can the quadrupole-order effects alone (compare the blue dots and black dashed line in Fig. 4), and thus our “one-shot mergers” occur for a larger range of I_0 than do quadrupole-order “fast” mergers.

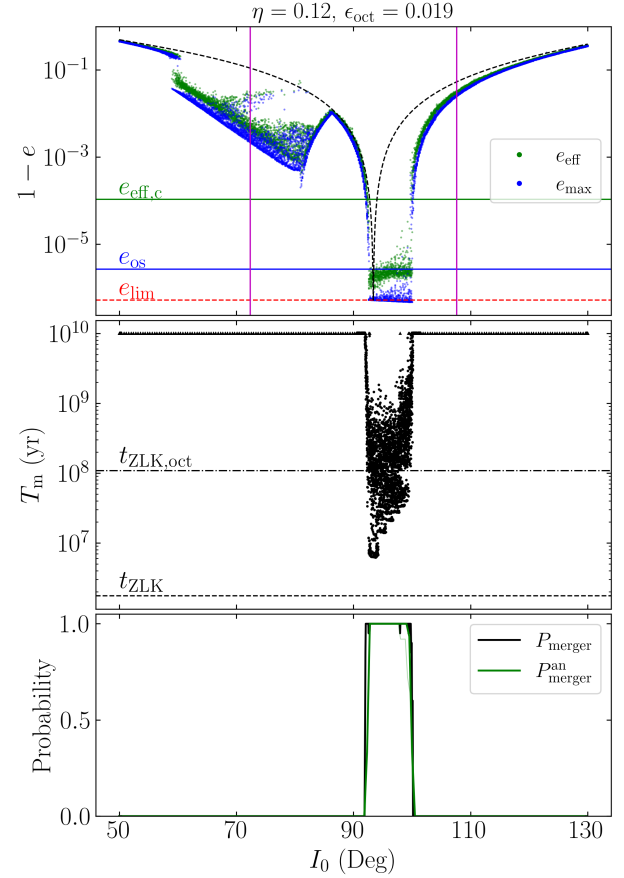


Figure 7. Same as Fig. 4 but for $e_{\text{out}} = 0.9$ while holding $a_{\text{out,eff}}$ the same, corresponding to $\eta = 0.118$ and $\epsilon_{\text{oct}} = 0.019$.

where the notation $P_{\text{merger}}(I_0; q, e_{\text{out}})$ highlights the dependence of P_{merger} on q and e_{out} , two of the key factors that determine the strength of the octupole effect (of course P_{merger} depends on other system parameters such as m_{12} , a_0 , a_{out} , etc.). The bottom panels of Figs. 4–8 show our numerical results. In all of these plots, there is a retrograde inclination window for which successful merger is guaranteed. In Fig. 5, it can be seen that a large range of prograde inclinations have a probabilistic outcome. In Fig. 6, while the enhanced octupole strength allows for most of the prograde inclinations to merge with certainty, there is still a region around $I_0 \approx 80^\circ$ where $P_{\text{merger}} < 1$.

3.2 Merger Probability: Semi-analytic Criteria

By comparing the top and bottom panels of Figs. 4–8, it is clear that their features are correlated: in all five cases, the retrograde merger window occupies the same inclination range as the retrograde octupole-active window, while P_{merger} is only nonzero for prograde inclinations where e_{max} nearly attains e_{lim} . Here, we further develop this connection and show that the non-dissipative simulations can be used to predict the outcomes of simulations with GW dissipation rather reliably.

In Section 3.1, we identified both one-shot and smooth mergers in our simulations. Towards understanding the one-shot mergers, we first define e_{os} to be the e_{max} required to dissipate an order-unity fraction of the binary’s orbital energy via GW emission in a single

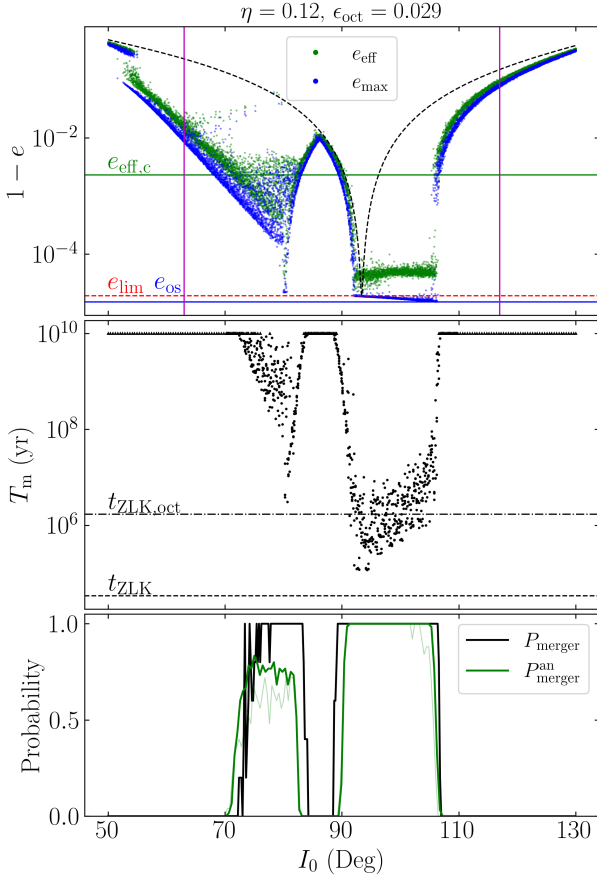


Figure 8. Same as Fig. 4 but for a more compact inner binary; the parameters are $a_0 = 10$ AU, $a_{\text{out,eff}} = 700$ AU, $m_{12} = 50M_\odot$, $m_3 = 30M_\odot$, $e_{\text{out}} = 0.9$, and $q = 0.4$, corresponding to $\eta = 0.118$ and $\epsilon_{\text{oct}} = 0.029$. Here, P_{merger} is computed with only 5 integrations (for random ω , ω_{out} , and Ω) for each I_0 .

ZLK cycle. Since a binary spends a fraction $\sim j(e_{\text{max}})$ of each ZLK cycle near e_{max} (e.g., Anderson et al. 2016), we set

$$j(e_{\text{os}}) \left. \frac{d \ln a}{dt} \right|_{e=e_{\text{os}}} = -\frac{1}{t_{\text{ZLK}}}, \quad (17)$$

where $d(\ln a)/dt$ is given by Eq. (13). This yields

$$j^6(e_{\text{os}}) \equiv \frac{425 t_{\text{ZLK}}}{96 t_{\text{GW},0}} = \frac{170}{3} \frac{G^3 \mu m_{12}^3}{m_3 c^5 a^4 n} \left(\frac{a_{\text{out,eff}}}{a} \right)^3, \quad (18)$$

where $t_{\text{GW},0} = (t_{\text{GW}})_{e=0}$ (see Eq. 13) is given by

$$t_{\text{GW},0}^{-1} = \frac{64}{5} \frac{G^3 \mu m_{12}^2}{c^5 a^4}, \quad (19)$$

we have approximated $e_{\text{os}} \approx 1$. Eq. (18) is equivalent to

$$1 - e_{\text{os}} \approx 3 \times 10^{-6} \left(\frac{m_{12}}{50M_\odot} \right)^{7/6} \left(\frac{q/(1+q)^2}{1/4} \right)^{1/3} \left(\frac{m_3}{30M_\odot} \right)^{-1/3} \times \left(\frac{a_{\text{out,eff}}}{3600 \text{ AU}} \right) \left(\frac{a}{100 \text{ AU}} \right)^{-11/6}. \quad (20)$$

Then, if a system satisfies $e_{\text{max}} > e_{\text{os}}$ with e_{max} based on non-dissipative integration, it is expected attain a sufficiently large eccentricity to undergo a one-shot merger.

Towards understanding smooth mergers, we seek a characteristic

eccentricity that captures GW emission over many ZLK cycles. We define e_{eff} as an effective ZLK maximum eccentricity, i.e.

$$\begin{aligned} \left\langle \frac{d \ln a}{dt} \right\rangle &= -\frac{1}{t_{\text{GW},0}} \left\langle \frac{1 + 73e^2/24 + 37e^4/96}{j^7(e)} \right\rangle \\ &\equiv -\frac{425/96}{t_{\text{GW},0}} \frac{1}{j^6(e_{\text{eff}})}, \end{aligned} \quad (21)$$

where the angle brackets denote averaging over many $t_{\text{ZLK,oct}}$ in order to capture the characteristic eccentricity behavior over many octupole cycles. In the second line of Eq. (21), we have essentially replaced the ZLK-averaged orbital decay rate by $d(\ln a)/dt$ evaluated at e_{eff} multiplied by $j(e_{\text{eff}})$. In practice (see Figs. 4–8), we typically average over $2000 t_{\text{ZLK}}$ of the non-dissipative simulations to compute e_{eff} .

With e_{eff} computed using Eq. (21), we can define the critical effective eccentricity $e_{\text{eff,c}}$ such that the ZLK-averaged inspiral time is a Hubble time, i.e. $\langle d(\ln a)/dt \rangle \equiv -(10 \text{ Gyr})^{-1}$. This gives

$$j^6(e_{\text{eff,c}}) \equiv \frac{425}{96} \frac{10 \text{ Gyr}}{t_{\text{GW},0}}, \quad (22)$$

or equivalently

$$1 - e_{\text{eff,c}} \approx 10^{-4} \left(\frac{m_{12}}{50M_\odot} \right) \left(\frac{q/(1+q)^2}{1/4} \right)^{1/3} \left(\frac{a}{100 \text{ AU}} \right)^{-4/3}. \quad (23)$$

Thus, if a system is evolved using the non-dissipative equations of motion and satisfies $e_{\text{eff}} > e_{\text{eff,c}}$, then it is expected to successfully undergo a smooth merger within a Hubble time.

Therefore, a system can be predicted to merge successfully if it satisfies either the one-shot or smooth merger criteria. The semi-analytical merger probability (as a function of I_0 and other parameters) is:

$$P_{\text{merger}}^{\text{pan}}(I_0; q, e_{\text{out}}) = P(e_{\text{eff}} > e_{\text{eff,c}} \text{ or } e_{\text{max}} > e_{\text{os}}). \quad (24)$$

Although not fully analytical (since numerical integrations of non-dissipative systems are needed to obtain e_{eff} and e_{max} in general), Eq. (24) provides efficient computation of the merger probability without full numerical integrations including GW radiation.

The top panels of Figs. 4–8 show e_{eff} and e_{max} , and their critical values, $e_{\text{eff,c}}$ and e_{os} . Using these, we compute the semi-analytical merger probability, shown as the thick green lines in the bottom panels of Figs. 4–8. We generally observe good agreement with the numerical P_{merger} . However, $P_{\text{merger}}^{\text{pan}}$ slightly but systematically underpredicts P_{merger} for some configurations, such as the prograde inclinations in Figs. 5 and 8. These regions coincide with the inclinations for which the merger outcome is uncertain. This underprediction is due to the restricted integration time of $2000 t_{\text{ZLK}} \approx 3$ Gyr used for the non-dissipative simulations. To illustrate this, we also calculate $P_{\text{merger}}^{\text{pan}}$ using a shorter integration time of $500 t_{\text{ZLK}}$ for our non-dissipative simulations. The results are shown as the light green lines in the bottom panels of Figs. 4–8, performing visibly worse. A more detailed discussion of this issue can be found in Section 4.4.

A few observations about Eq. (24) can be made. First, it explains why some prograde systems merge probabilistically ($0 < P_{\text{merger}} < 1$): for the prograde inclinations in Fig. 5, the e_{eff} values scatter widely around $e_{\text{eff,c}}$ [or more precisely, $j(e_{\text{eff}})$ scatters around $j(e_{\text{eff,c}})$], even for a given I_0 , so the detailed merger outcome depends on the initial conditions. For the prograde inclinations in Fig. 6, the double-valued feature in the e_{max} plot (the top panel) pointed out in Section 2.3 represents a sub-population of systems that do not satisfy Eq. (24). Second, $e_{\text{max}} > e_{\text{os}}$ often ensures $e_{\text{eff}} > e_{\text{eff,c}}$ in practice, as the averaging in Eq. (21) is heavily weighted towards

extreme eccentricities. As such, $e_{\text{eff}} > e_{\text{eff},c}$ alone is often a sufficient condition in Eq. (24).

The one-shot merger criterion ($e_{\text{max}} > e_{\text{os}}$) can also be used to distinguish two different types of system architectures: if $e_{\text{lim}} \gtrsim e_{\text{os}}$ for a particular architecture, then all initial conditions leading to orbit flips (i.e., in an octupole-active window) also execute one-shot mergers. For $e_{\text{lim}} \approx 1$, Eq. (9) reduces to

$$j(e_{\text{lim}}) \approx \frac{8\epsilon_{\text{GR}}}{9} \left(1 + \frac{\eta^2}{12}\right)^{-1}. \quad (25)$$

which lets us rewrite the constraint $e_{\text{lim}} \gtrsim e_{\text{os}}$ as

$$\left(\frac{a}{a_{\text{out,eff}}}\right) \gtrsim 0.0186 \left(\frac{a_{\text{out,eff}}}{3600 \text{ AU}}\right)^{-7/37} \left(\frac{m_{12}}{50M_{\odot}}\right)^{17/37} \times \left(\frac{30M_{\odot}}{m_3}\right)^{10/37} \left(\frac{q/(1+q)^2}{1/4}\right)^{-2/37}. \quad (26)$$

For the system architecture considered in Figs. 4–7, this condition is satisfied, and we see indeed that wherever the top panel suggests orbit flipping ($e_{\text{max}} = e_{\text{lim}}$), the bottom panel shows $P_{\text{merger}} \approx 1$. When the condition (Eq. 26) is not satisfied, one-shot mergers are not possible, and P_{merger} is generally only nonzero for a small range about $I_{0,\text{lim}}$.

4 MERGER FRACTION AS A FUNCTION OF MASS RATIO

Having developed an semi-analytical understanding of the binary merger window and probability in the last section (particularly Section 3.2), we now study the fraction of BH binaries in triples that successfully merge under various conditions – we call this the merger fraction.

4.1 Merger Fraction for Fixed Tertiary Eccentricity

We first consider the simple case where e_{out} is fixed at a few specific values and compute the merger fraction as a function of the mass ratio q . We consider isotropic mutual orientations between the inner and outer binaries, i.e. we draw $\cos I_0$ from a uniform grid over the range $[-1, 1]$ (recall that ω , ω_{out} , and Ω are drawn uniformly from the range $[0, 2\pi]$ when computing the merger probability P_{merger} at a given I_0). The merger fraction is then given by:

$$f_{\text{merger}}(q, e_{\text{out}}) \equiv \frac{1}{2} \int_{-1}^1 d\cos I_0 P_{\text{merger}}(I_0; q, e_{\text{out}}). \quad (27)$$

This is proportional to the integral of the black lines (weighted by $\sin I_0$) in the bottom panels of Figs. 4–7. We can also use semi-analytical criteria introduced in Section 3.2 to predict the outcome and merger fraction. This is computed by using $P_{\text{merger}}^{\text{an}}$ as the integrand in Eq. (27), or by evaluating the integral of the thick green lines (weighted by $\sin I_0$) in the bottom panels of Figs. 4–7. Figure 9 shows the resulting f_{merger} and the analytical estimates for all combinations of $q \in \{0.2, 0.3, 0.4, 0.5, 0.7, 1.0\}$ and $e_{\text{out}} \in \{0.6, 0.8, 0.9\}$. It is clear that the numerical f_{merger} and the analytical estimate agree well, and that the merger fraction increases steeply for smaller q .

To explore the impact of our choice of isotropic mutual orientations between the two binaries, we also consider a wedge-shaped distribution of $\cos I_0$ as was found in the population synthesis studies of Antonini et al. (2017). We still use the same uniform grid of $\cos I_0$

as before, but weight each eccentricity by its probability density following the distribution:

$$P(\cos I_0) = \frac{1}{4} + \frac{|\cos I_0|}{2}. \quad (28)$$

The resulting f_{merger} for a tertiary with $\cos I_0$ distributed like Eq. (28) is shown as the dashed lines in Fig. 9. While the total merger fractions decrease, the strong enhancement of the merger fraction at smaller q is unaffected.

In the right panel of Fig. 9, we see that the merger fractions for the three e_{out} values overlap for small ϵ_{oct} . This implies that f_{merger} depends only on ϵ_{oct} in this regime, and not on the values of q and e_{out} independently. From Fig. 4 (which has $\epsilon_{\text{oct}} = 0.007$), we see that this suggests that the size of the retrograde merger window only depends on ϵ_{oct} , much like what Eq. (12) shows for the test-particle limit. However, once ϵ_{oct} is increased sufficiently, the three curves in the right panel of Fig. 9 cease to overlap. This can be attributed to their different η values: for sufficiently small ϵ_{oct} , no prograde initial inclinations successfully merge (e.g., Fig. 4), and the merger fraction is solely determined by the size of the retrograde octupole-active window. But once ϵ_{oct} is sufficiently large, prograde mergers become possible, and the merger fraction is also affected by the size of the octupole-inactive gap, which depends on η . This again illustrates the importance of the octupole-inactive gap, which we comment on in Appendix A.

Figure 10 depicts the merger fractions for systems with $a_0 = 50$ AU (the other parameters are the same as in Fig. 9). According to Eq. (26), these systems no longer satisfy $e_{\text{lim}} \gtrsim e_{\text{os}}$, so the merger fraction is expected to diminish strongly and vary much more weakly with q , as one-shot mergers are no longer possible. This is indeed observed, particularly for the $e_{\text{out}} = 0.6$ curve in Fig. 10. We also remark that the semi-analytical prediction accuracy is poorer in this case than in Fig. 9. This is because the only mergers in this regime are smooth mergers. As can be seen for the prograde I_0 in Figs. 5 and 8, smooth mergers occur over a wide range of merger times T_m , and the specific T_m that a system experiences depends sensitively on its chaotic evolution. Thus, Eq. (21) is a rather approximate estimate of the amount of GW emission that a real system emits during a smooth merger; indeed, the prograde regions of Figs. 5 and 8 show that the merger times for smooth mergers are systematically underpredicted by the semi-analytic merger criterion (see discussion in Section 4.4). The non-monotonicity of the semi-analytic merger fraction for $e_{\text{out}} = 0.6$ from $q = 0.2$ to $q = 0.3$ is due to small sample sizes and finite grid spacing in $\cos I_0$.

4.2 Merger Fraction for a Distribution of Tertiary Eccentricities

For a distribution of tertiary eccentricities, denoted $P(e_{\text{out}})$, the merger fraction is given by

$$\begin{aligned} \eta_{\text{merger}}(q) &= \int de_{\text{out}} P(e_{\text{out}}) f_{\text{merger}}(q, e_{\text{out}}), \\ &= \int de_{\text{out}} \frac{P(e_{\text{out}})}{2} \int_{-1}^1 d\cos I_0 P_{\text{merger}}(I_0; q, e_{\text{out}}). \end{aligned} \quad (29)$$

We consider two possible $P(e_{\text{out}})$ with $e_{\text{out}} \in [0, 0.9]$: (i) a uniform distribution, $P(e_{\text{out}}) = \text{constant}$, and (ii) a thermal distribution, $P(e_{\text{out}}) \propto e_{\text{out}}$.

The top panel of Fig. 11 shows η_{merger} (black dots) for the fiducial triple systems (with the same parameters as in Figs. 4–7). For each q ,

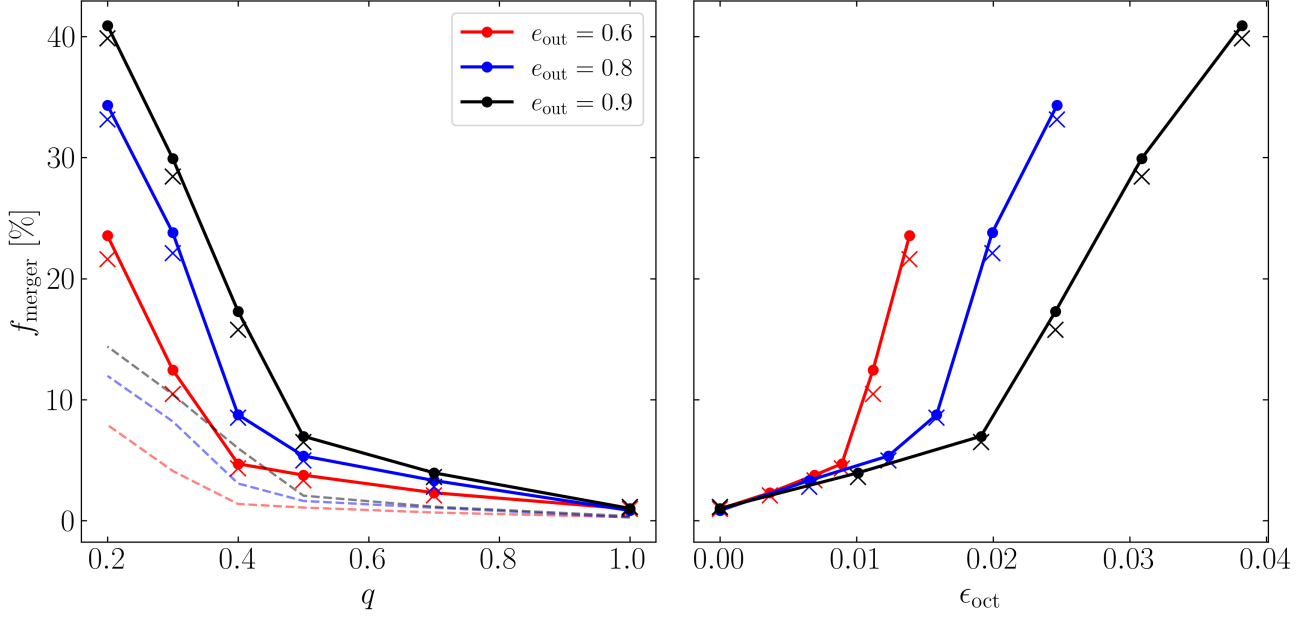


Figure 9. Merger fraction (Eq. 16) of BH binaries in triples as a function of mass ratio q (left panel) for several values of outer binary eccentricities. The other system parameters are the same as in Figs. 4–7. The right panel shows the same merger fraction, but plotted against the octupole parameter ϵ_{oct} . The filled circles joined by the solid lines are numerical results (based on integrations for full triple system evolution including GW emission; see the black solid lines in the bottom panels of Figs. 4–7) assuming random mutual inclinations between the inner and outer binaries (uniform in $\cos I_0$), and the dashed lines denote the merger fractions if the mutual inclinations are distributed according to Eq. (28). The crosses are semi-analytical results using an integration time of $2000t_{\text{ZLK}}$ (see the thick green lines in the bottom panels of Figs. 4–7).

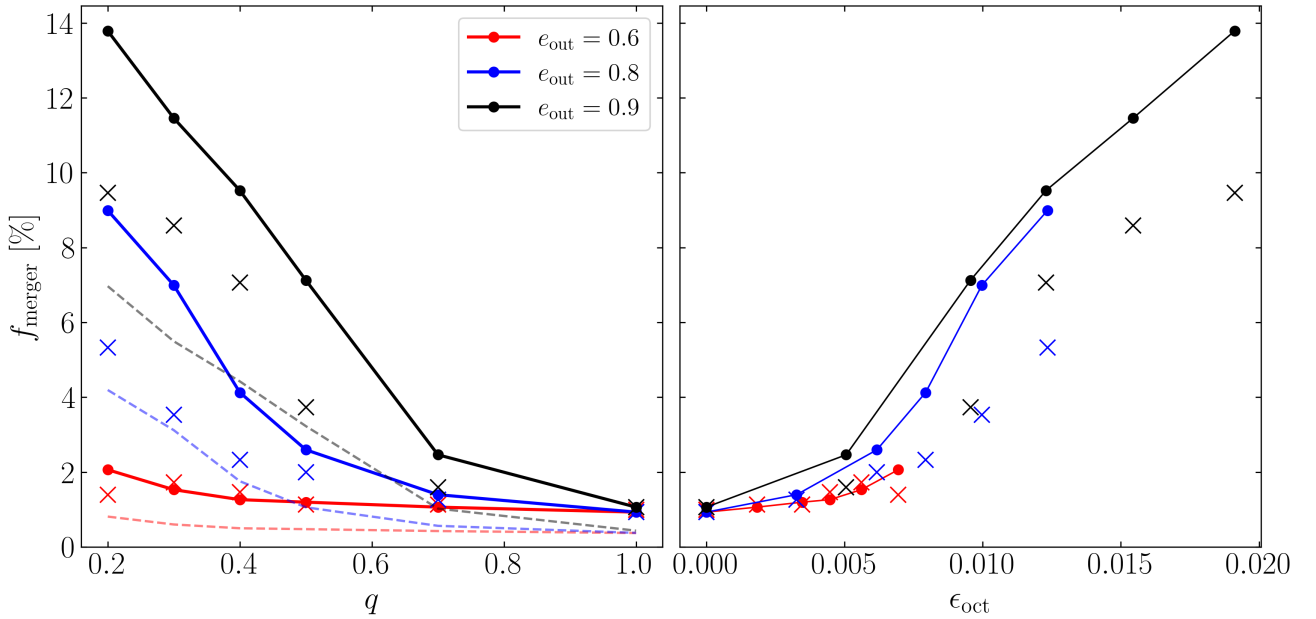


Figure 10. Same as Fig. 9 but for $a_0 = 50$ AU.

the integral in Eq. (29) is computed using 1000 realizations of random e_{out} , $\cos I_0$, ω , ω_{out} , and Ω . Not surprisingly, we see η_{merger} increases with decreasing q . When q is small, a thermal distribution of e_{out} tends to yield higher η_{merger} than does a uniform distribution. We also compute the merger fraction using the semi-analytical merger probability of Eq. (24) on a dense grid of initial conditions uniformly sampled in e_{out} and $\cos I_0$; the result is shown as the blue dotted line in Fig. 11, which is in good agreement with the uniform- e_{out} simulation result (black).

To characterize the properties of merging binaries, the middle and bottom panels of Fig. 11 show the distributions of merger times and merger eccentricities (at both the LISA and LIGO bands) for different mass ratios. To obtain the LISA and LIGO band eccentricities (with GW frequency equal to 0.1 Hz and 10 Hz respectively), the inner binaries are evolved from when they reach $0.005a_0$ (at which point we terminate the integration of the triple system evolution as the inner binary's evolution is decoupled from the tertiary; see Eq. 15) to physical merger using Eqs. (13–14). While the LIGO band eccentricities are all quite small ($\lesssim 10^{-3}$), the LISA band eccentricities (at 0.1 Hz) are significant, with median $\gtrsim 0.2$ for $q \lesssim 0.5$. We note that these eccentricities are generally smaller than those found in the population studies of Liu et al. (2019a). This is because in this paper we consider only sufficiently hierarchical systems for which double-averaged evolution equations are valid, whereas Liu et al. (2019a) included a wider range of triple hierarchies and had to use N -body integrations to evolve some of the systems.

For comparison, Figure 12 shows the results when $a_{\text{out,eff}} = 5500$ AU (instead of $a_{\text{out,eff}} = 3600$ AU for Fig. 11) with all other parameters unchanged. While η_{merger} is lower than it is for $a_{\text{out,eff}} = 3600$ AU, there is still a large increase of η_{merger} with decreasing q . Since Eq. (26) is still satisfied, this is expected.

4.3 $q \ll 1$ Limit

For fixed m_{12} (and other parameters), even though the octupole strength ϵ_{oct} increases as q decreases, the efficiency of GW radiation also decreases. It is therefore natural to ask at what q these competing effects become comparable and the merger fraction is maximized. We show that this does not happen until q is extremely small.

We see from Figs. 4–7 that $e_{\text{lim}} > e_{\text{os}}$ for our fiducial triple systems. Indeed, from Eq. (26), we see that even for q as small as 10^{-5} , the condition $e_{\text{lim}} > e_{\text{os}}$ is satisfied. This implies that most binaries execute one-shot mergers when undergoing an orbit flip. In addition, recall that the characteristic time for the binary to approach e_{lim} can be estimated by Eq. (11), which, for our fiducial triple systems, is given by

$$t_{\text{ZLK,oct}} \simeq 10^8 \left(\frac{m_{12}}{50M_{\odot}} \right)^{1/2} \left(\frac{a_{\text{out,eff}}}{3600 \text{ AU}} \right)^{7/2} \left(\frac{a}{100 \text{ AU}} \right)^{-2} \times \left(\frac{m_3}{30M_{\odot}} \right)^{-1} \left[\frac{1-q}{1+q} \frac{e_{\text{out}}}{\sqrt{1-e_{\text{out}}^2}} \right]^{-1/2} \text{ yr.} \quad (30)$$

Since $t_{\text{ZLK,oct}} \ll 10$ Gyr, this implies that the octupole-ZLK-induced binary merger fractions are primarily determined by what initial conditions would lead to extreme eccentricity excitation and only weakly depend on the GW radiation rate. Indeed, Eq. (26) shows that, while $e_{\text{lim}} > e_{\text{os}}$ is indeed violated if q is decreased sufficiently, the dependence is extremely weak. Thus, η_{merger} is expected to be very nearly constant for all physically relevant values of q , as can be seen in Fig. 13.

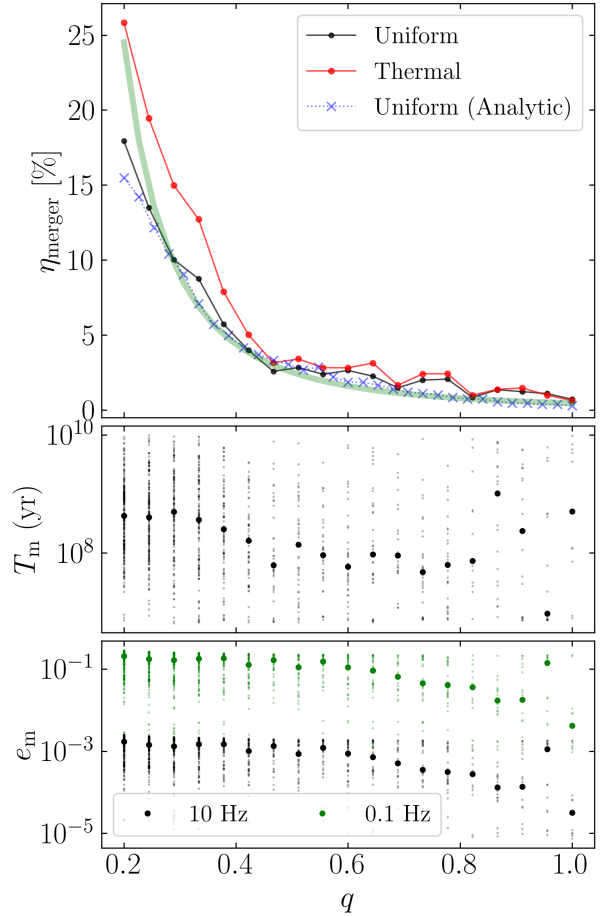


Figure 11. *Upper panel:* Binary BH merger fraction as a function of mass ratio q for the fiducial triple systems (with parameters the same as in Figs. 4–7), assuming random mutual inclinations (uniform in $\cos I_0$), and either uniform (black dots) or thermal distribution (red dots) for the tertiary eccentricity distribution [with $e_{\text{out}} \in [0, 0.9]$]. These are obtained numerically using Eq. (29) by sampling 1000 combinations of e_{out} , $\cos I_0$, ω , ω_{out} , and Ω . The blue dotted line is the semi-analytical result obtained by applying Eq. (24) in Eq. (29) (evaluated using a dense uniform grid of $\cos I_0$ and e_{out}). The thick green line is a power-law fit to the analytical η_{merger} with a power law index of -2.5 . *Middle panel:* Merger times of successful mergers for a uniform e_{out} distribution (the median is denoted with the large black dot). *Bottom panel:* Merging binary eccentricities (again, for a uniform e_{out} distribution) in the LISA band (0.1 Hz; green) and in the LIGO band (10 Hz; black), with medians marked with large dots.

4.4 Limitations of semi-analytic Calculation

It can be seen in Fig. 9 that the semi-analytical merger fractions are systematically lower than the values obtained from the direct simulations. One reason that this discrepancy arises is because the non-dissipative simulations used to compute e_{eff} and e_{max} are only run for $2000t_{\text{LK}} \approx 3$ Gyr, while the full simulations including GW dissipation are run for 10 Gyr. Owing to the chaotic nature of the octupole-order ZLK effect, this means that, if an initial condition leads to extreme eccentricities only after many Gyrs, then e_{eff} and e_{max} are underpredicted by the non-dissipative simulations. Additionally, there are times when eccentricity vector of the inner binary is librating, during which orbit flips are strongly suppressed

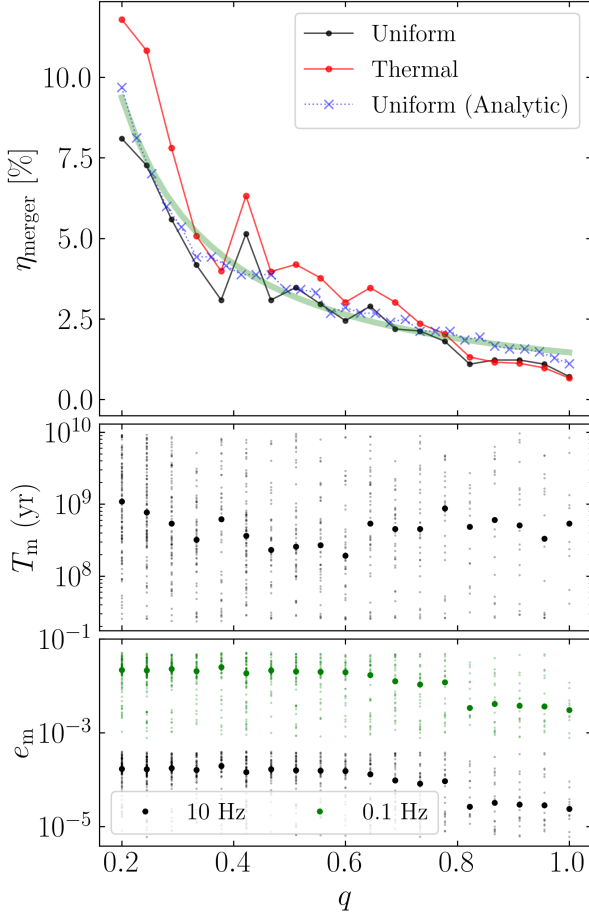


Figure 12. Same as Fig. 11 but for $a_{\text{out,eff}} = 5500$ AU. The power law index of the fit to the analytical η_{merger} is -1.15 .

(Katz et al. 2011). Since the librating phase can last an unpredictable amount of time, this suggests that the semi-analytical merger criteria can become more complete as the integration time is increased.

We quantify the “completeness” of the semi-analytical merger fraction via the ratio $f_{\text{merger}}^{\text{an}}/f_{\text{merger}}$ as a function of non-dissipative integration time. We focus on the fiducial triple systems for demonstrative purposes and compute the completeness for each of the q and e_{out} combinations shown in Fig. 9. Figure 14 shows the completeness for each of these simulations in light grey lines and their mean in the thick black line. We see that the completeness is still increasing even as the non-dissipative simulation time is increased to $2000t_{\text{ZLK}}$, so we expect that even longer integration times would give even better agreement with the dissipative simulations.

5 MASS RATIO DISTRIBUTION OF MERGING BH BINARIES

In Section 4, we have calculated the binary BH merger fractions f_{merger} and η_{merger} as a function of the mass ratio q for some representative triple systems. To determine the distribution in q and m_{12} (total mass) of the merging binaries, we would need to know both the initial distribution in q , m_{12} and a_0 of the inner BH binaries and the

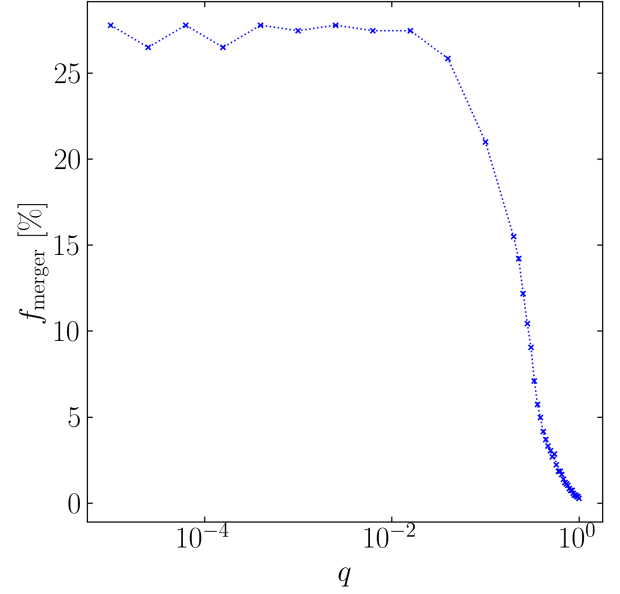


Figure 13. Same as blue dashed line of the top panel of Fig. 11 but extended to very small q . Due to the very weak q dependence in Eq. (26), f_{merger} is expected to depend very weakly on q when $q \ll 1$ (such that e_{out} is approximately constant), which agrees with the simulation results.

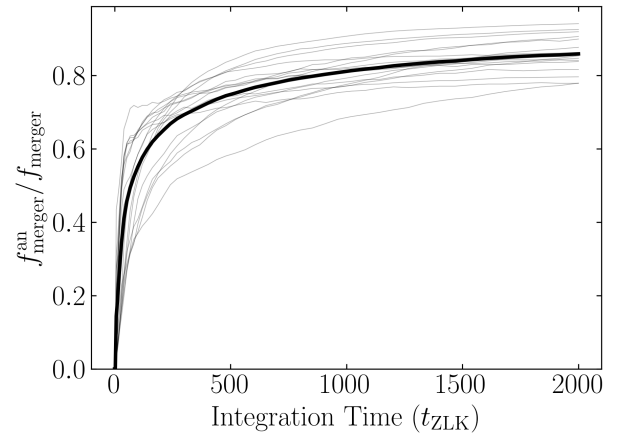


Figure 14. Completeness of the semi-analytical merger fraction, defined as $f_{\text{merger}}^{\text{an}}/f_{\text{merger}}$, as a function of the integration time used for the non-dissipative simulations, in the fiducial parameter regime while e_{out} is fixed at a few values. The thin grey lines indicate the completeness for particular combinations of (q, e_{out}) , and the thick black line denotes their average. We see that completeness is still increasing as the integration time approaches $2000t_{\text{ZLK}} \approx 3$ Gyr.

distribution in m_3 , a_{out} and e_{out} of the outer binaries, denoted by:

$$\frac{dF}{dq dm_{12} da_0}, \quad \frac{dF_{\text{out}}}{dm_3 da_{\text{out}} de_{\text{out}}}. \quad (31)$$

The distribution in q and m_{12} of the merging binaries is then

$$\frac{dF_{\text{merger}}}{dq dm_{12}} = \int da_0 dm_{\text{out}} da_{\text{out}} de_{\text{out}} \frac{dF}{dq dm_{12} da_0} \times \frac{dF_{\text{out}}}{dm_3 da_{\text{out}} de_{\text{out}}} f_{\text{merger}}(q, e_{\text{out}}; m_{12}, a_0, m_3, a_{\text{out}}, e_{\text{out}}), \quad (32)$$

where f_{merger} is given by Eq. (27) (assuming random mutual inclinations between the inner and outer binaries), and we have spelled out its dependence on various system parameters. Some examples of f_{merger} are shown in Figs. 9–10. If we further specify the eccentricity distribution of the outer binaries, we have

$$\frac{dF_{\text{merger}}}{dq dm_{12}} = \int da_0 dm_3 da_{\text{out}} \frac{dF}{dq dm_{12} da_0} \times \frac{dF_{\text{out}}}{dm_3 da_{\text{out, eff}}} \eta_{\text{merger}}(q; m_{12}, a_0, m_3, a_{\text{out, eff}}), \quad (33)$$

where η_{merger} is given by Eq. (29). Some examples of η_{merger} are shown in the top panels of Figs. 11–12.

Clearly, to properly evaluate Eq. (32) or (33) would require large population synthesis calculations and in any case would involve significant uncertainties, a task beyond the scope of this paper. For illustrative purposes, we consider the fiducial triple systems as studied in Section 4, and estimate the mass-ratio distribution of BH mergers as

$$\frac{dF_{\text{merger}}}{dq} \sim \frac{dF}{dq} \eta_{\text{merger}}(q). \quad (34)$$

5.1 Initial q -distribution of BH Binaries

The initial mass-ratio distribution of BH binaries, dF/dq , is uncertain. It can be derived from the the mass distributions of of main-sequence (MS) binaries, together with the MS mass (m_{ms}) to BH mass (m) relation.

For the distribution of MS binary masses, we assume that each MS component mass is drawn from a Salpeter-like initial mass function (IMF) independently, with

$$\frac{dF_{\text{ms}}}{dm_{\text{ms}}} \propto m_{\text{ms}}^{-\alpha}, \quad (35)$$

in the range $m_{\text{min}} \leq m_{\text{ms}} \leq m_{\text{max}}$. Note in this case the MS binary mass-ratio distribution is (for $q \leq 1$)

$$\frac{dF_{\text{ms}}}{dq} \propto q^{\alpha-2} \left[1 - \left(\frac{q}{q_{\text{min}}} \right)^{2-2\alpha} \right], \quad (36)$$

where $q_{\text{min}} = m_{\text{min}}/m_{\text{max}}$ is the minimum possible binary mass ratio (this is a generalization of the result of Tout 1991). We consider two representative values of α : (i) $\alpha = 2.35$, the canonical Salpeter IMF (Salpeter 1955), and (ii) $\alpha = 2$, resulting in a uniform q distribution (for $q \geq 2q_{\text{min}}$). The latter case is consistent with observational studies of the mass ratio of high-mass MS binaries (Sana et al. 2012; Duchêne & Kraus 2013; Kobulnicky et al. 2014; Moe & Di Stefano 2017).

To obtain dF/dq , we compute the BH binary mass ratio when each main sequence mass m_{ms} is mapped to its corresponding BH mass m . This mapping is taken from Spera & Mapelli (2017) for the mass range $25M_{\odot} \leq m_{\text{ms}} \leq 117M_{\odot}$. We consider both the case where $Z = 0.02$ (“high Z ”) and where $Z = 2.0 \times 10^{-4}$ (“low Z ”), the two limiting metallicities used in Spera & Mapelli (2017). We can then numerically compute dF/dq by sampling masses for stellar binaries from the IMF, translating these into BH masses, then calculating the

resulting BH mass ratios for each binary. The upper panel of Fig. 15 shows the dF/dq obtained via this procedure for a Salpeter IMF ($\alpha = 2.35$) when sampling 10^5 MS binaries for each metallicity. In the lower four panels, we also show dF/dq restricted to particular ranges of m_{12} . Note that the distributions differ significantly among the m_{12} ranges and also between the two metallicities. Figure 16 shows the case when $\alpha = 2$, which mostly resembles Fig. 15.

5.2 q -distribution of Merging BH Binaries

Using the results of Section 5.1, we can also estimate the mass ratio distribution of merging BHs using Eq. (34). We consider representative triple systems considered in Section 4: for η_{merger} , we use a simple approximation that lies roughly between the two cases shown in Figs. 11–12:

$$\eta_{\text{merger}}(q) \approx 0.2 \times [\max(q, 0.2)]^{-2}. \quad (37)$$

The results for dF_{merger}/dq are displayed as the dotted curves in Figs. 15–16 in each panel. Broadly speaking, dF_{merger}/dq peaks around $q \sim 0.3$ for low- Z systems, and around $q \sim 0.4$ for high- Z systems, the latter reflecting the peak in the initial BH binary q -distribution. Also note that dF_{merger}/dq can be quite different for different m_{12} ranges. For example, merging BH binaries with $m_{12} > 42M_{\odot}$ are only produced in low- Z systems, and dF_{merger}/dq peaks around $q \sim 0.3$ for $m_{12} \in [42, 67]M_{\odot}$, and is roughly uniform between $q \sim 0.2$ to 1 for $m_{12} \geq 67M_{\odot}$.

We emphasize that these results for dF_{merger}/dq refer to the representative triple systems studied in Sections 2–4, and thus should be considered for illustrative purposes only. As noted above, the merger fraction η_{merger} depends on various parameters of the triple systems. While we have not attempted to quantify η_{merger} for all possible triple system parameters, it is clear that the principal finding of Section 4 (i.e., η_{merger} increases with decreasing q) applies only for systems with sufficiently strong octupole effects. In fact, from Figs. 9 and 10 we can estimate that the octupole-induced feature in η_{merger} becomes prominent only when $\epsilon_{\text{oct}} \gtrsim 0.005$, or equivalently

$$\frac{a}{a_{\text{out, eff}}} \gtrsim 0.005 \left(\frac{1+q}{1-q} \right) \frac{\sqrt{1-e_{\text{out}}^2}}{e_{\text{out}}} \approx \frac{0.01}{e_{\text{out}}}, \quad (38)$$

where in the second step we have used $q \sim 0.5$ and $e_{\text{out}} \sim 0.6$. When this condition is satisfied, the inner binary can usually also undergo a one-shot merger (see Eq. 26), leading to strong dependence of the merger fraction on q . For triple systems with $a/a_{\text{out, eff}} \lesssim 0.01$ (such as the case when the tertiary is a supermassive BH with $m_3 \gtrsim 10^6 m_{12}$), the octupole effect is unimportant (see the discussion following Eq. 2), and we expect the merger fraction to be almost independent of q . Indeed, an analytical fitting formula for BH mergers induced by pure quadrupole-ZLK effect shows $\eta_{\text{merger}} \propto \mu^{0.16} \propto q^{0.16}/(1+q)^{0.32}$ (see Eq. 53 of Liu & Lai 2018, or Eq. 26 of Liu & Lai 2021). For such systems, we expect dF_{merger}/dq to be mainly determined by the initial q -distribution of BH binaries at their formation.

6 SUMMARY AND DISCUSSION

We have studied the dynamical formation of merging BH binaries induced by a tertiary companion via the von Zeipel-Lidov-Kozai (ZLK) effect, focusing on the expected mass ratio distribution of merging binaries. The octupole potential of the tertiary, when sufficiently

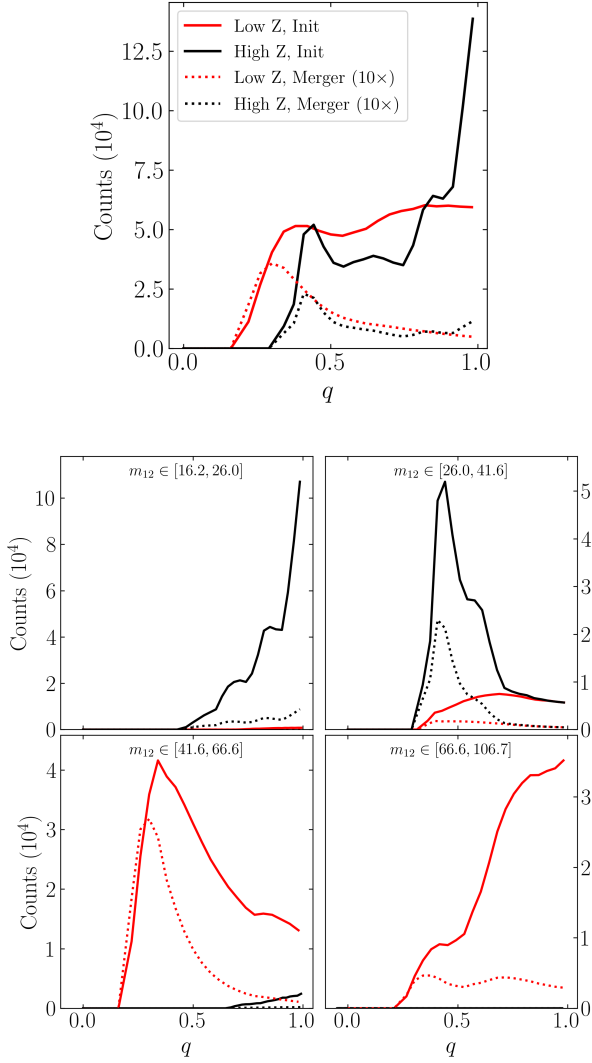


Figure 15. Mass ratio distributions of the initial BH binaries (solid lines) and merging BH binaries (dotted lines) when using $\alpha = 2.35$ for the MS stellar initial mass function (see Sections 5.1 and 5.2). *Top panel:* Distribution of binary mass ratio at formation and merger for all possible total binary BH masses. Each BH mass is obtained from the MS mass using the fitting formula of [Spera & Mapelli \(2017\)](#) for metallicities of 2×10^{-4} (Low Z) and 0.02 (High Z), while the merger fraction of BH binaries is given by Eq. (37). To produce these distributions, 10^5 initial MS binaries are used for each metallicity, and the number of merging BH binaries has been scaled up by a factor of 10 for visibility. The counts refer to the number per $\Delta q = 0.05$ bin. *Bottom four panels:* Same as the top panel but with specific ranges of m_{12} , the total BH mass of the binary (as labeled). Note that low- m_{12} systems are mainly produced from high-Z MS binaries, while high- m_{12} systems are mainly produced in low-Z MS binaries.

strong, can increase the inclination window and probability of extreme eccentricity excitation, and thus enhance the rate of successful binary mergers. Since the octupole strength $\epsilon_{\text{oct}} \propto (1-q)/(1+q)$ (see Eq. 2) increases with decreasing binary mass ratio q , it is expected that ZLK-induced BH mergers favor binaries with smaller mass ratios. We quantify the dependence of the merger fraction/probability on q using a combination of numerical integrations and analytical calculations, based on the secular evolution equations for hierarchical

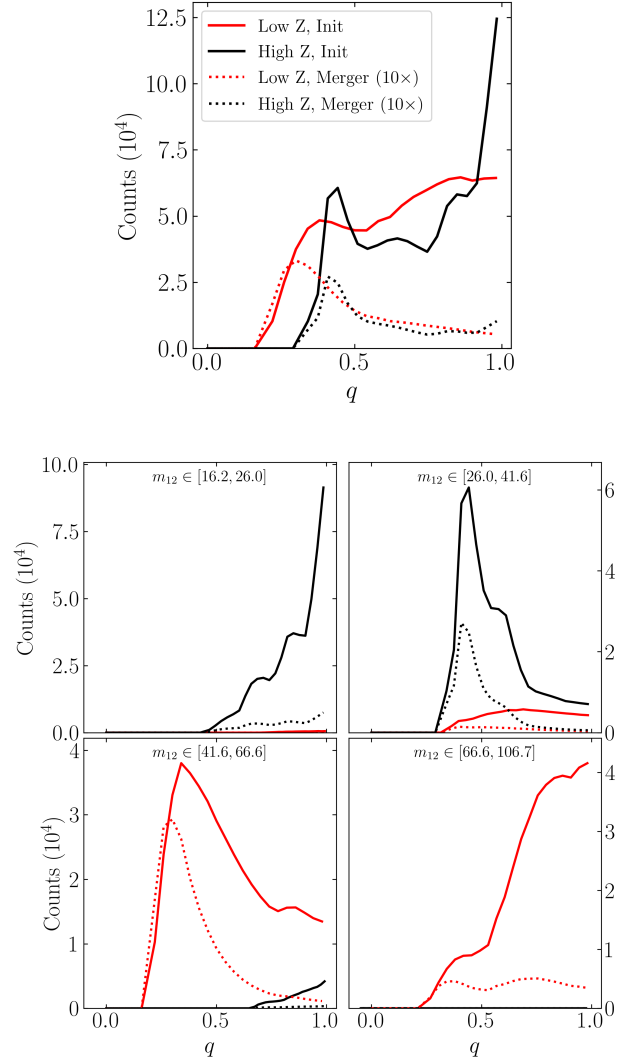


Figure 16. Same as Fig. 15 but for $\alpha = 2$, i.e. a nearly uniform distribution of the main sequence binary mass ratio. The results are very similar to Fig. 15.

triples. We develop new analytical criteria (Section 3.2) that allow us to determine, without full numerical integrations, whether an initial BH binary can undergo a “one-shot merger” or a more gradual merger under the influence of a tertiary companion. These allow us to compute the merger probability semi-analytically by only studying non-dissipative (i.e. no GWs) triple systems (see Eq. 24). We show that for hierarchical triples with semi-major axis ratio $a/a_{\text{out}} \gtrsim 0.01 - 0.02$ (see Eq. 38), the BH binary merger fraction (f_{merger} or η_{merger}) can increase by a larger factor (up to ~ 20) as q decreases from unity to 0.2 (see Figs. 9–13). When combined with a reasonable estimate of the mass ratio distribution of the initial BH binaries (Section 5.1), our results for the merger fraction suggest that the final merging BH binaries have an overall mass ratio distribution that peaks around $q = 0.3$ or 0.4 , although very different distributions can be produced when restricting to specific ranges of total binary masses (see Figs. 15 and 16).

Taking our final results (Figs. 15 and 16) at face value, we tentatively conclude that the mass-ratio distribution dF_{merger}/dq of BH binary mergers induced by a comparable-mass companion is incon-

sistent with the current LIGO/VIRGO result (see Fig. 1), suggesting that such tertiary-induced mergers may not be the dominant formation channel for the majority of the detected LIGO/VIRGO events. However, there are at least two important issues/caveats to keep in mind:

(i) dF_{merger}/dq depends strongly on the initial mass-ratio distribution of BH binaries at their formation (dF/dq), which is uncertain and depends sensitively on the metallicity of the binary formation environment (see Section 5.1). It is also possible that the initial BH binary mass ratio distribution is much more skewed towards equal masses than what we found in Section 5.1 (e.g. if stellar binaries with significantly asymmetric masses become unbound due to mass loss and supernova kicks as their components become BHs). Such a distribution was found by population synthesis studies that include octupole-order ZLK effects and models of stellar evolution (e.g. [Hamers et al. 2013](#); [Toonen et al. 2018](#)). These studies find that ZLK oscillations in stellar binaries with small q can experience mass transfer and merge without forming a compact object binary; as a result, most compact object binaries form with large mass ratios. The prevalence of this phenomenon likely depends on the initial semi-major axes of the inner binaries. Further study would be required to understand the competition between this primordial large- q enhancement and the elevated merger fractions for small q found in the present study in an astrophysically realistic population.

(ii) When the tertiary mass m_3 is much larger than the BH binary mass m_{12} , as in the case of a supermassive BH tertiary, dynamical stability of the triple requires $a_{\text{out}} \gg a$, which implies that the octupole effect is negligible ($\epsilon_{\text{oct}} \ll 1$). For such triple systems, we expect the merger fraction to depend very weakly on the mass ratio, and the final dF_{merger}/dq to depend entirely on the initial dF/dq . Although the merger fraction of such “pure quadrupole” triples is small ($\leq 6\%$; see Eq. 53 of [Liu & Lai 2018](#)), additional “external” effects can enhance the merger efficiency significantly [e.g., when the outer orbit experiences quasi-periodic torques from the galactic potential ([Petrovich & Antonini 2017](#); see also [Hamers & Lai 2017](#)), or from the spin of a supermassive BH ([Liu et al. 2019b](#))].

Near the completion of this paper, we became aware of the simultaneous work by [Martinez et al. \(2021\)](#), who study a similar topic using a population synthesis approach.

7 ACKNOWLEDGEMENTS

We thank the anonymous referee whose detailed review and comments greatly improved this paper. YS thanks Jiseon Min for useful discussions. This work has been supported in part by NSF grant AST1715246. YS is supported by the NASA FINESST grant 19-ASTRO19-0041. BL gratefully acknowledges support from the European Union’s Horizon 2020 research and innovation program under the Marie Skłodowska-Curie grant agreement No. 847523 ‘INTER-ACTIONS’.

8 DATA AVAILABILITY

The data referenced in this article will be shared upon reasonable request to the corresponding author.

REFERENCES

Abbott R., et al., 2020a, arXiv preprint arXiv:2010.14533
Abbott R., et al., 2020b, *The Astrophysical Journal Letters*, 900, L13

Anderson K. R., Storch N. I., Lai D., 2016, *Monthly Notices of the Royal Astronomical Society*, 456, 3671
Antognini J. M., 2015, *Monthly Notices of the Royal Astronomical Society*, 452, 3610
Antonini F., Perets H. B., 2012a, *The Astrophysical Journal*, 757, 27
Antonini F., Perets H. B., 2012b, *The Astrophysical Journal*, 757, 27
Antonini F., Murray N., Mikkola S., 2014, *The Astrophysical Journal*, 781, 45
Antonini F., Toonen S., Hamers A. S., 2017, *The Astrophysical Journal*, 841, 77
Antonini F., Rodriguez C. L., Petrovich C., Fischer C. L., 2018, *Monthly Notices of the Royal Astronomical Society: Letters*, 480, L58
Banerjee S., Baumgardt H., Kroupa P., 2010, *Monthly Notices of the Royal Astronomical Society*, 402, 371
Belczynski K., Dominik M., Bulik T., O’Shaughnessy R., Fryer C., Holz D. E., 2010, *The Astrophysical Journal Letters*, 715, L138
Belczynski K., Holz D. E., Bulik T., O’Shaughnessy R., 2016, *Nature*, 534, 512
Blaes O., Lee M. H., Socrates A., 2002, *The Astrophysical Journal*, 578, 775
Dominik M., Belczynski K., Fryer C., Holz D. E., Berti E., Bulik T., Mandel I., O’Shaughnessy R., 2012, *The Astrophysical Journal*, 759, 52
Dominik M., Belczynski K., Fryer C., Holz D. E., Berti E., Bulik T., Mandel I., O’Shaughnessy R., 2013, *The Astrophysical Journal*, 779, 72
Dominik M., et al., 2015, *The Astrophysical Journal*, 806, 263
Downing J., Benacquista M., Giersz M., Spurzem R., 2010, *Monthly Notices of the Royal Astronomical Society*, 407, 1946
Duchêne G., Kraus A., 2013, *Annual Review of Astronomy and Astrophysics*, 51, 269
Ford E. B., Kozinsky B., Rasio F. A., 2000, *The Astrophysical Journal*, 535, 385
Fragione G., Bromberg O., 2019, *Monthly Notices of the Royal Astronomical Society*, 488, 4370
Fragione G., Kocsis B., 2019, *Monthly Notices of the Royal Astronomical Society*, 486, 4781
Fragione G., Loeb A., 2019, *Monthly Notices of the Royal Astronomical Society*, 486, 4443
Gerosa D., Berti E., O’Shaughnessy R., Belczynski K., Kesden M., Wysocki D., Gladysz W., 2018, *Phys. Rev. D*, 98, 084036
Gondán L., Kocsis B., Raffai P., Frei Z., 2018, *The Astrophysical Journal*, 860, 5
Hamers A. S., 2020a, *Monthly Notices of the Royal Astronomical Society*, 494, 5492
Hamers A. S., 2020b, *Monthly Notices of the Royal Astronomical Society*, 500, 3481
Hamers A. S., Lai D., 2017, *Monthly Notices of the Royal Astronomical Society*, 470, 1657
Hamers A. S., Pols O. R., Claeys J. S. W., Nelemans G., 2013, *MNRAS*, 430, 2262
Hoang B.-M., Naoz S., Kocsis B., Rasio F. A., Dosopoulou F., 2018, *The Astrophysical Journal*, 856, 140
Katz B., Dong S., Malhotra R., 2011, *Physical Review Letters*, 107, 181101
Kinoshita H., 1993, *Celestial Mechanics and Dynamical Astronomy*, 57, 359
Kiseleva L. G., Aarseth S. J., Eggleton P. P., de La Fuente Marcos R., 1996, in Milone E. F., Mermilliod J. C., eds, *Astronomical Society of the Pacific Conference Series Vol. 90, The Origins, Evolution, and Destinies of Binary Stars in Clusters*. p. 433
Kobulnicky H. A., et al., 2014, *The Astrophysical Journal Supplement Series*, 213, 34
Kozai Y., 1962, *The Astronomical Journal*, 67, 591
Lei H., Circi C., Ortore E., 2018, *Monthly Notices of the Royal Astronomical Society*, 481, 4602
Li G., Naoz S., Holman M., Loeb A., 2014, *The Astrophysical Journal*, 791, 86
Lidov M. L., 1962, *Planetary and Space Science*, 9, 719
Lipunov V., Postnov K., Prokhorov M., 1997, *Astronomy Letters*, 23, 492
Lipunov V., et al., 2017, *Monthly Notices of the Royal Astronomical Society*, 465, 3656
Lithwick Y., Naoz S., 2011, *The Astrophysical Journal*, 742, 94

- Liu B., Lai D., 2017, *The Astrophysical Journal Letters*, 846, L11
- Liu B., Lai D., 2018, *The Astrophysical Journal*, 863, 68
- Liu B., Lai D., 2019, *Monthly Notices of the Royal Astronomical Society*, 483, 4060
- Liu B., Lai D., 2020, *Physical Review D*, 102, 023020
- Liu B., Lai D., 2021, *Monthly Notices of the Royal Astronomical Society*, 502, 2049
- Liu B., Muñoz D. J., Lai D., 2015, *Monthly Notices of the Royal Astronomical Society*, 447, 747
- Liu B., Lai D., Wang Y.-H., 2019a, *The Astrophysical Journal*, 881, 41
- Liu B., Lai D., Wang Y.-H., 2019b, *The Astrophysical Journal Letters*, 883, L7
- Luo L., Katz B., Dong S., 2016, *Monthly Notices of the Royal Astronomical Society*, 458, 3060
- Martinez M. A., Rodriguez C. L., Fragione G., 2021, arXiv preprint arXiv:2105.01671
- Miller M. C., Hamilton D. P., 2002, *The Astrophysical Journal*, 576, 894
- Miller M. C., Lauburg V. M., 2009, *The Astrophysical Journal*, 692, 917
- Moe M., Di Stefano R., 2017, *The Astrophysical Journal Supplement Series*, 230, 15
- Muñoz D. J., Lai D., Liu B., 2016, *Monthly Notices of the Royal Astronomical Society*, 460, 1086
- Naoz S., 2016, *Annual Review of Astronomy and Astrophysics*, 54, 441
- O’leary R. M., Rasio F. A., Fregeau J. M., Ivanova N., O’Shaughnessy R., 2006, *The Astrophysical Journal*, 637, 937
- Olejak A., Fishbach M., Belczynski K., Holz D. E., Lasota J.-P., Miller M. C., Bulik T., 2020, *The Astrophysical Journal*, 901, L39
- Peters P. C., 1964, *Physical Review*, 136, B1224
- Petrovich C., Antonini F., 2017, *The Astrophysical Journal*, 846, 146
- Podsiadlowski P., Rappaport S., Han Z., 2003, *Monthly Notices of the Royal Astronomical Society*, 341, 385
- Portegies Zwart S. F., McMillan S. L. W., 2000, *ApJ*, 528, L17
- Randall L., Xianyu Z.-Z., 2018a, *The Astrophysical Journal*, 853, 93
- Randall L., Xianyu Z.-Z., 2018b, *The Astrophysical Journal*, 864, 134
- Rodet L., Su Y., Lai D., 2021, *The Astrophysical Journal*, 913, 104
- Rodriguez C. L., Morscher M., Pattabiraman B., Chatterjee S., Haster C.-J., Rasio F. A., 2015, *Physical Review Letters*, 115, 051101
- Rodriguez C. L., Chatterjee S., Rasio F. A., 2016, *Physical Review D*, 93, 084029
- Rodriguez C. L., Amaro-Seoane P., Chatterjee S., Rasio F. A., 2018, *Physical Review Letters*, 120, 151101
- Salpeter E. E., 1955, *The Astrophysical Journal*, 121, 161
- Samsing J., D’Orazio D. J., 2018, *Monthly Notices of the Royal Astronomical Society*, 481, 5445
- Samsing J., Ramirez-Ruiz E., 2017, *The Astrophysical Journal Letters*, 840, L14
- Sana H., et al., 2012, *Science*, 337, 444
- Shevchenko I. I., 2016, *The Lidov-Kozai effect-applications in exoplanet research and dynamical astronomy. Astrophysics and Space Science Library Vol. 441*, Springer
- Silsbee K., Tremaine S., 2017, *The Astrophysical Journal*, 836, 39
- Spera M., Mapelli M., 2017, *Monthly Notices of the Royal Astronomical Society*, 470, 4739
- Su Y., Lai D., Liu B., 2021, *Physical Review D*, 103, 063040
- Toonen S., Perets H., Hamers A., 2018, *Astronomy & Astrophysics*, 610, A22
- Tout C. A., 1991, *Monthly Notices of the Royal Astronomical Society*, 250, 701
- von Zeipel H., 1910, *Astronomische Nachrichten*, 183, 345
- Wen L., 2003, *The Astrophysical Journal*, 598, 419
- Ziosi B. M., Mapelli M., Branchesi M., Tormen G., 2014, *Monthly Notices of the Royal Astronomical Society*, 441, 3703

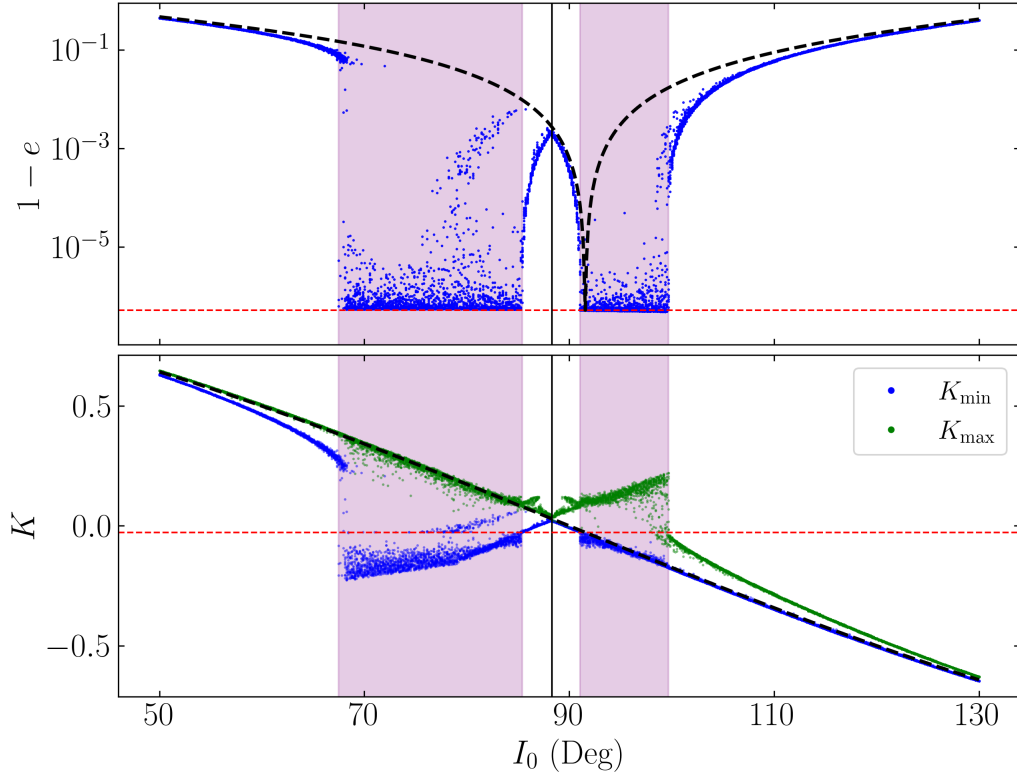


Figure A1. Octupole-active windows and amplitude of oscillation of K (Eq. 4). *Top panel:* Maximum eccentricity e_{max} attained by the inner binary with initial tertiary inclination I_0 when integrated for $2000t_{\text{ZLK}}$ (blue dots), reproduced from the top panel of Fig. 6. Also shown are e_{lim} (Eq. 9, horizontal red dashed line), the quadrupole-level result for e_{max} (Eq. 7, dashed black line), the empirically-determined center of the gap, located at $I_0 \approx 88.32^\circ$ (vertical black line), and the inclinations that can lead to extreme eccentricities (shaded purple regions). *Bottom panel:* Minimum and maximum values of K , denoted K_{min} and K_{max} , attained by the systems. Also shown are the initial K for a given I_0 (black dashed line) and the critical $K_c = -\eta/2$ for orbit flipping (horizontal red dashed line). The center of the octupole-inactive gap and the octupole-active windows are labeled as in the top panel.

APPENDIX A: ORIGIN OF OCTUPOLE-INACTIVE GAP

We investigate the origin of the “octupole-inactive gap”, an inclination range near $I_0 \approx 90^\circ$ for which e_{max} does not attain e_{lim} despite being in between two octupole-active windows. This gap was first identified in Section 2.3, and is seen in both the non-dissipative and full simulations with GW dissipation (see Figs. 4–8).

To better understand this gap, we first review the mechanism by which extreme eccentricity excitation occurs. In the test-particle limit, Katz et al. (2011) showed that K (Eq. 4) oscillates over long timescales when ω , the argument of pericenter of the inner orbit, is circulating. This then leads to orbit flips (and extreme eccentricity excitation) between prograde and retrograde inclinations when K changes signs: since $j(e)$ is nonnegative, the sign of K determines the sign of $\cos I$. Katz et al. (2011) obtained coupled oscillation equations in K and Ω_e , the azimuthal angle of the inner eccentricity vector in the inertial reference frame. The amplitude of oscillation of K can then be analytically computed, and the octupole-active window (the range of I_0 over which orbit flips occur) is the region for which the range of these oscillations encompasses $K = 0$ (Katz et al. 2011). When ω is librating instead, Ω_e jumps by $\sim 180^\circ$ every ZLK cycle, and the oscillations in K are suppressed.

In the finite- η case, we commented in Section 2.3 that the relation between K oscillations and extreme eccentricity excitation (and orbit flipping) can be generalized even when η is nonzero. K still oscillates over timescales $\gg t_{\text{ZLK}}$ when ω is circulating, and if its range of oscillation contains $K_c \equiv -\eta/2$, then the inner orbit flips, in the process attaining extreme eccentricities. To be precise, orbit flips are defined to be when the range of inclination oscillations changes from $(\cos I_0)_- < \cos I < \cos I_{0,\text{lim}}$ to $\cos I_{0,\text{lim}} < \cos I < (\cos I_0)_+$ or vice versa, where $(\cos I_0)_\pm$ are given by Eq. (10) and $I_{0,\text{lim}}$ satisfies Eq. (8).

However, the range of oscillation of K is more complex than it is in the test-particle limit. Figure A1 compares the behavior of e_{max} in the non-dissipative simulations (top panel; reproduced from the top panel of Fig. 6) to the range of oscillations in K (bottom panel). Denote the center of the gap $I_{0,\text{gap}}$ (shown as the vertical black line in both panels of Fig. A1). Near $I_{0,\text{gap}}$, K oscillates about $K(I_{0,\text{gap}})$, which is *positive*, and the oscillation amplitude goes to zero at $I_{0,\text{gap}}$. On the other hand, orbit flips (and extreme eccentricity excitation) are possible when the range of oscillation of K encloses K_c (i.e., $K_{\text{min}} < K_c < K_{\text{max}}$). The purple shaded regions in both panels of Fig. A1 illustrate this equivalence, as they show both the e_{lim} -attaining inclinations in the top panel and the inclinations where $K_{\text{min}} < K_c < K_{\text{max}}$ in the bottom panel. But since $K(I_{0,\text{gap}}) > 0$ while $K_c < 0$, there will always be a range of I_0 about $I_{0,\text{gap}}$ for which the oscillation amplitude is smaller than $K(I_{0,\text{gap}}) - K_c$, and orbit flips are impossible in this range. This range then corresponds to the octupole-inactive gap.

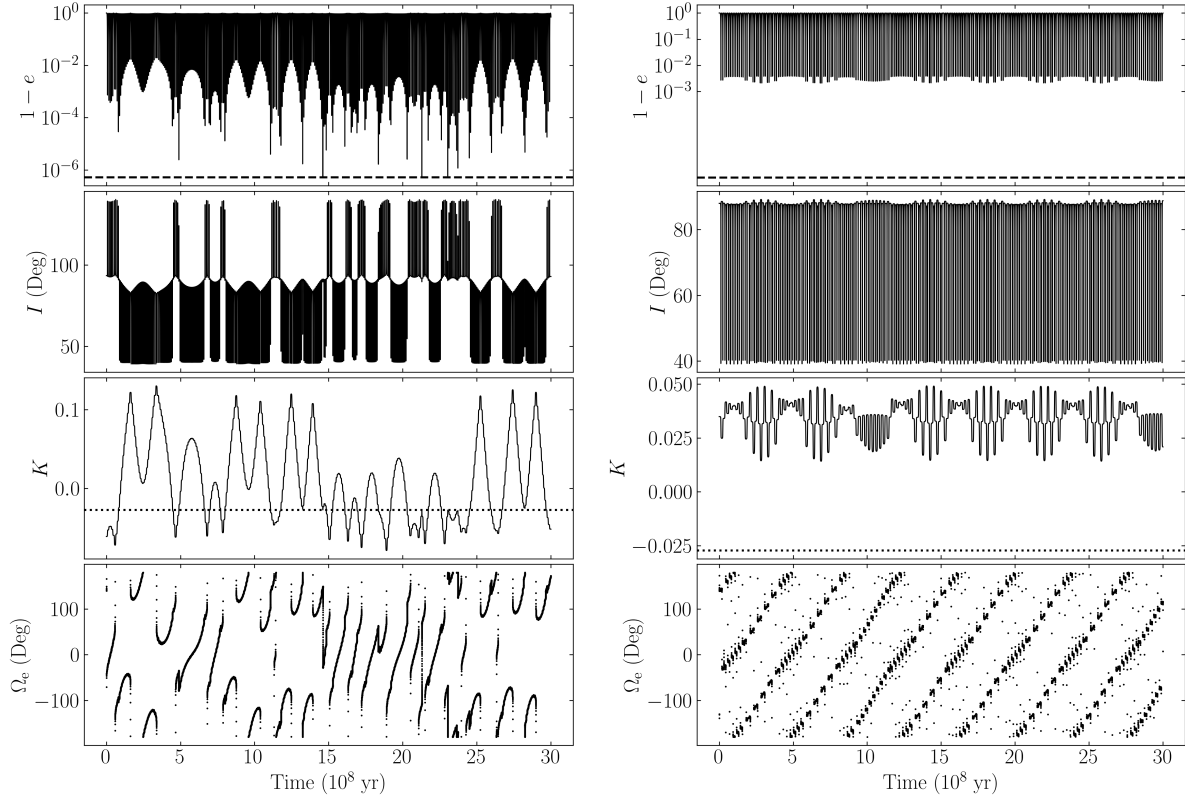


Figure A2. The left panel is the same as Fig. 3 but includes the evolution of the azimuthal angle of the eccentricity vector, Ω_e . The right panel is the same as the left but for $I_0 = 88^\circ$. For both of these examples, we have used $\omega_0 = 0$, but the evolution is similar for all ω_0 .

This analysis has simply pushed our lack of understanding onto a new quantity: why are K oscillations suppressed in the neighborhood of $I_{0,\text{gap}}$? A quantitative answer to this question is beyond the scope of this paper, but for a qualitative understanding, we can examine the evolution of a system in the octupole-inactive gap. The left panel of Fig. A2 shows the same simulation as Fig. 3 but with an additional panel showing Ω_e , while the right panel shows a simulation with the same parameters except $I_0 = 88^\circ$, which is near $I_{0,\text{gap}}$ (see Fig. A1). The oscillations in K (third panels) are much smaller for $I_0 = 88^\circ$ than for $I_0 = 93.5^\circ$, and no orbit flips occur. Most interestingly, the fourth panel shows that the evolution of Ω_e is much less smooth than in Fig. 3, jumping at almost every other eccentricity maximum. Katz et al. (2011) have already pointed out that jumps in Ω_e occur when ω is *librating*, rather than *circulating*.

When the octupole-order terms are neglected, the circulation-libration boundary is a boundary in e - ω space: as long as the ZLK separatrix exists in the e - ω plane and $e_0 > 0$, then an initial $\omega_0 = 0$ causes ω to circulate, while an initial $\omega_0 = \pi/2$ causes ω to librate (e.g., Kinoshita 1993; Shevchenko 2016). However, when including octupole-order terms, this picture breaks down. To illustrate this, for a range of I_0 and both $\omega_0 = 0$ and $\omega_0 = \pi$, we evolve the fiducial system parameters for a single ZLK cycle, using $q = 0.2$ as is used for Figs. A1 and A2, and consider both the dynamics with and without the octupole-order terms. Figure A3 gives the resulting changes in Ω_e over a single ZLK period when the octupole-order effects are neglected (top) and when they are not (bottom). Two observations can be made: (i) $I_{0,\text{gap}}$ is approximately where $\Delta\Omega_e = 0$ for circulating initial conditions when neglecting octupole-order terms, and (ii) the inclusion of the octupole-order terms seem to cause Ω_e to exclusively vary slowly ($|\Delta\Omega_e| \ll 180^\circ$) except for $I_{0,\text{gap}} < I_0 < I_{0,\text{lim}}$. The former is plausible: if $K(I_{0,\text{gap}})$ is the location of an equilibrium in K - Ω_e space, then it must satisfy $\Delta\Omega_e = 0$. The latter suggests that the assumption of circulation of ω in Katz et al. (2011) may be satisfied for many more initial conditions than the quadrupole-level analysis suggests, as long as they are not in octupole-inactive gap.

Finally, examination of the bottom panel of Fig. A1 suggests that the oscillation amplitude in K grows roughly linearly with $|I_0 - I_{0,\text{gap}}|$ in the vicinity of $I_{0,\text{gap}}$ (this may be because, in the test-particle limit, librating ω give oscillation amplitudes in K that are higher-order in K and Ω_e , as pointed out by Katz et al. 2011). Assuming this, the gap width can then be given by

$$\text{Gap Width} = 2 \left(I_{0,\text{lim}} - I_{0,\text{gap}} \right). \quad (\text{A1})$$

This explains why the gap does not exist in the test-particle regime, as $I_{0,\text{lim}} = I_{0,\text{gap}} = 90^\circ$ by symmetry of the equations of motion.

It is clear from the preceding discussion and Fig. A3 that the octupole-order, finite- η dynamics are complex, and our discussion can only be considered heuristic. Nevertheless, in the absence of a closed form solution to the octupole-order ZLK equations of motion or a full generalization of the work of Katz et al. (2011), they provide a preliminary understanding of the octupole-inactive gap.

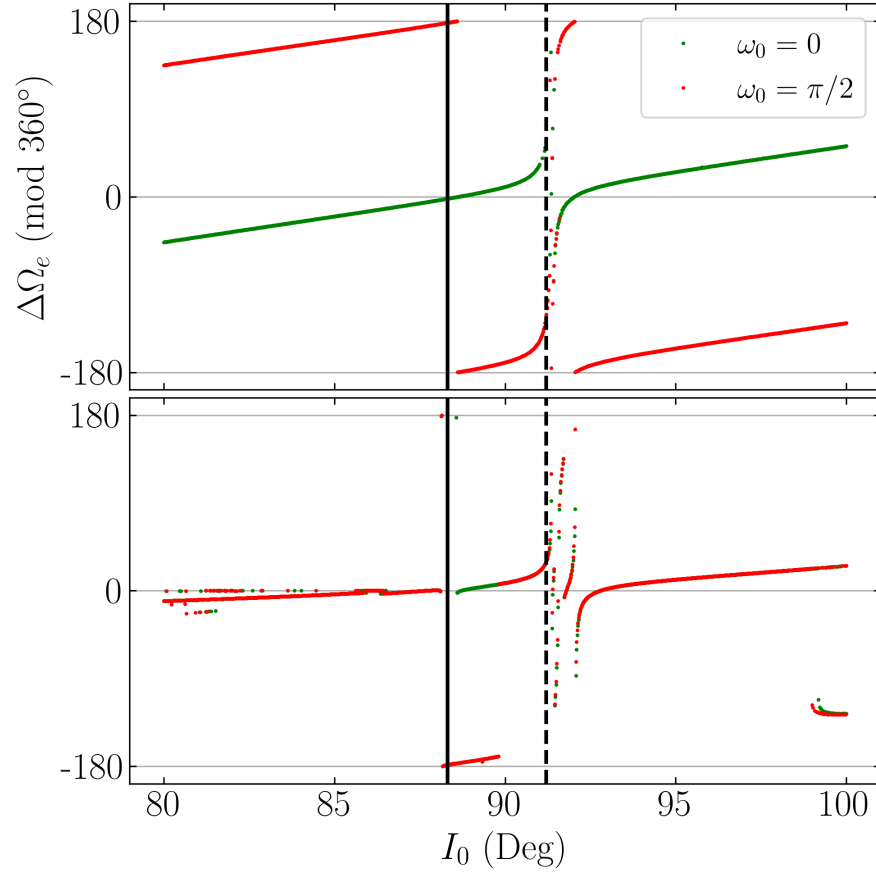


Figure A3. Plot of $\Delta\Omega_e$, the change in Ω_e over a single ZLK cycle, for $q = 0.2$ and the fiducial parameters using different initial conditions. In the top panel, octupole-order terms are neglected, while in the lower panel, they are not. The solid and dashed vertical black lines denote $I_{0,\text{gap}}$ and $I_{0,\text{lim}}$ respectively.